NUMERICAL SIMULATION OF PLASMA ASSISTED TURBULENT COMBUSTION

BY

ANAND SRINIVAS ANKALA

A THESIS PRESENTED TO THE GRADUATE SCHOOL
OF THE UNIVERSITY OF FLORIDA IN PARTIAL FULFILLMENT OF THE
REQUIREMENTS FOR THE
DEGREE OF MASTER OF SCIENCE

UNIVERSITY OF FLORIDA

2011

This document is dedicated to my parents who have supported me in all my endeavors.

ACKNOWLEDGMENTS

First of all, I would like to thank Dr. Subrata Roy, the chairman of my graduate committee, for providing me with an opportunity to work under his guidance as a part of his research group. Dr. Roy shared with me his extensive knowledge and always motivated me to perform better. I would also be grateful to Dr. William Lear and Dr. Corin Segal, for accepting to be members in my committee. I would like to thank Dr. Chin Chen Wang for his every help in successful completion of my thesis.

In addition, I would like to thank Navya, Jignesh, Tomas, Mark, Ankush, Ariel, Moses, members of CPDLT lab and my friends, Uday, Abhijyoth and Bhageerath for their academic help.

Above all I would like to express my gratitude to my parents for their unwavering support and blessings.

TABLE OF CONTENTS

page

LIST OF TABLES

LIST OF FIGURES

LIST OF KEY SYMBOLS

C_s Model constant

F Electrodynamic force (N)

h Enthalpy (kJ/kg)

k Turbulent kinetic energy (J)

l_t Turbulent length scale (m)

r Radius (m)

Re Reynolds number

S Shear stress (N/m^2)

Sc_k Schmidt number

t Time (s)

u Velocity (m/s)

Y Mixture fraction

Δ Grid Size (m)

Greek Letters

β Function of dielectric material

ϵ Dissipation rate (m^2/s^2)

ν Kinematic viscosity (m^2/s)

τ Timescale (s)

ρ Density (kg/m^3)

ν_t Turbulent viscosity (m^2/s)

μ Absolute viscosity (kg/ms)

σ_k Turbulent Prandtl number for kinetic energy

σ_ϵ Turbulent Prandtl number for dissipation rate

η_k Kolmogorov length scale (m)

$\dot{\omega}$ Chemical reaction rate

ε Dielectric constant

ϕ Applied potential (v)

Subscripts

t Turbulent

k Kinetic energy

ϵ Dissipation rate

Abstract of Thesis Presented to the Graduate School
of the University of Florida in Partial Fulfillment of the
Requirements for the Degree of Master of Science

NUMERICAL SIMULATION OF PLASMA ASSISTED TURBULENT COMBUSTION

By

Anand Srinivas Ankala

August 2011

Chair: Subrata Roy
Major: Mechanical Engineering

Many attempts have been made to improve the performance of a gas turbine combustion chamber, and the area of turbulent combustion has been of keen interest to the research community in recent years. In particular, CFD simulations in this area have a significant importance, because of their accuracy being on par with the experiments and substantial reduction in the cost and time. The current work has focused on modification of the combustion of methane in a gas turbine combustion chamber by incorporating the fluid dynamic effects of a standard plasma actuator. Application of high voltage potential between two electrodes separated by a dielectric material produces an electric field that leads to the generation of plasma. This electric field couples to the plasma to create a body force, and by orienting the plasma force in the desired direction, the combustion rate can be accelerated by increasing the flame blow-off velocity. For the present study, the geometry was created in Gambit. All steady and transient simulations were carried out in Fluent employing turbulent models. Initially the effect of the plasma force was studied in the regime without any chemical reaction in the flow field. Non-premixed combustion of methane and air has been modeled and in the next stage, plasma force was applied to the system. The actuators are placed near the

regions where vortices are present in the flow field and the plasma force tends to break them down and at the same time the flow is accelerated and enhancement in the mixing of reactants is observed. An unsteady detached-eddy simulation has been performed to analyze the modifications in the flow field and combustion phenomenon created by the plasma force. A reduction in the amount of NO_x emissions has been observed after employing an empirical relation between flame temperature and the NO_x emissions index.

CHAPTER 1
INTRODUCTION

Combustion is the result of an exothermic chemical reaction between a fuel and an oxidant, where there is production of heat and conversion of reactants into new chemical species. Typical examples of oxidizers are oxygen and fluorine. Examples of practical fuels are organic compounds particularly hydrocarbons in gas, liquid or solid phase. The most ideal case is a complete combustion where the products are compounds of each element in the fuel with the oxidizing element. But in practice, complete combustion is impossible to achieve. Incomplete combustion occurs when there is no enough oxygen for the fuel (hydrocarbon) to produce carbon dioxide and water. For most fuels such as diesel, coal, pyrolysis occurs before combustion, which is thermo-chemical decomposition of organic matter at elevated temperatures in the absence of oxygen. In incomplete combustion, pyrolysis products are unburnt and they contaminate the smoke with hazardous particulate matter and gases. Hence there is a need to improve the quality of the combustion by better design of combustion devices. In the present work, an attempt has been made to study the combustion performance inside a gas turbine combustion chamber by employing a dielectric barrier discharge (DBD) plasma actuators to create turbulence in the flow field.

The dielectric barrier discharge (DBD) plasma actuator is a relatively simple device. In the recent years, it has received such attention due to its simplicity in design and operation. Technical details of the working of a plasma actuator have been cited from the work of Subrata Roy et al. [1]. A high voltage, alternating current (AC) source capable of peaks on the order of 5 to 10 kV are required for its operation. The high voltage signal is applied to a conducting electrode adhered to a dielectric substrate. A

grounded electrode is placed asymmetrically on the lower surface of the dielectric with an additional dielectric layer to avoid an unwanted discharge. The surrounding air is weakly ionized because of the high potential difference between the two electrodes. The plasma generated induces a body force on the fluid resulting in a tangential wall jet as shown in Figure 1-1. The induced flow, in quiescent air, is of a few meters per second. By applying an electric field, one can decrease the flame propagation velocity along a channel and even extinguish the flame [2] or accelerate the combustion rate by increasing the flame blow-off velocity [3]. More rapid combustion makes it possible to use leaner mixtures, which results in a decrease in the temperature of the combustion products and a reduction in the rate of NO_x production.

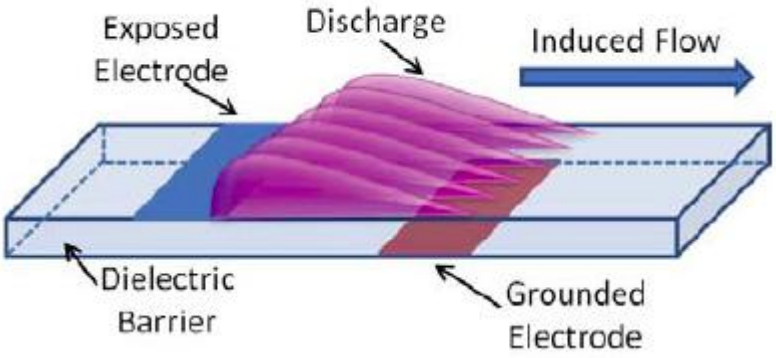

Figure 1-1. Generic (standard) linear dielectric barrier discharge plasma actuator

Modeling and meshing have been performed in Gambit, where as the simulations were carried out in Fluent. Steady and Transient simulations have been performed for the present study. The flame propagation has been simulated using a large eddy simulation (LES) model. LES has been preferred over the Reynolds averaged Navier Stokes (RANS) approach because of the following reasons.

In LES, the large and the energy-containing scales of motion are simulated numerically where as the small and unresolved sub-grid scales are modeled along with

their interaction with large scales. The former scales, which usually control the behavior and statistical properties of a turbulent flow, tend to be geometry and flow dependant. On the contrary, the small scales are more universal and consequently easier to model.

Application of LES has been questioned in the past stating that the chemical reactions occur only after the mixing of the reactants at the molecular level, turbulent reacting flows cannot be universal at the smallest scales and hence sub-grid models cannot be any simpler than in Reynolds averaged Navier-Stokes equation(RANS) approach. This argument has been negotiated by many researchers stating that presence of chemical reactions does not contradict the universality of small scales. Moreover, flamelet models of turbulent combustion presuppose that universal flame structures exist at the smallest scales. In fact, RANS approach fails to predict turbulent reacting flows accurately, so even with a simple chemistry model, LES outperforms RANS models that employ more sophisticated chemistry models.

Large eddy simulation has been in employment as turbulent flow prediction tool for engineering during the past few decades and with the advancement in computer technology and development of the dynamic sub-grid scale modeling procedure, there has been a significant progress. The advantage of dynamic sub-grid scale model is that model coefficients are automatically computed using the information contained in the resolved turbulent scales and hence eliminating the uncertainties. Reviews of LES are given by Lesieur et al. [4] and Moin et al. [5].

Experimental data for non-swirling and swirling confined coaxial jets with and without chemical reaction from the experiments conducted at United Technological Research Center by Johnson et al. [6], Owen et al. [7] has facilitated application of LES

to gas turbine combustor configurations. Simulation of an incompressible flow with a passive scalar in a non-swirling confined coaxial jet by Akselvoll et al. [8] obtained a good agreement with the experimental data of Johnson et al. [6]. Pierce et al. [9] have further extended the work by including the effect of swirl, which is commonly used in the design of the gas turbine combustors.

CHAPTER 2
THEORY

2.1 Combustion Concepts

2.1.1 Equivalence Ratio

Equivalence ratio is defined as the ratio of the fuel to oxidizer ratio to the stoichiometric fuel to oxidizer ratio.

2.1.2 Lean Mixture

A mixture is said to be a lean mixture if it has lesser fuel-air ratio compared to the stoichiometric fuel-air ratio.

2.1.3 Classification

Combustion is classified to be laminar or turbulent based on the Reynolds number of the flow of unburnt reactants entering the flame front.

2.1.4 Damkohler Number

Damkohler number (D_a) is defined as the ratio of the turbulent time scale to the chemical time scale.

If the Damkohler number is very small ($D_a << 1$), turbulence is much faster than the chemistry. The regime is the well stirred reactor, where products and reactants are rapidly mixed. If the Damkohler number is very large ($D_a >> 1$), chemical reaction occurs much faster than all turbulent scales. Turbulence does not alter the flame structure and the chemical region is laminar conditions.

Regimes for turbulent non-premixed combustion as a function of Damkohler number and turbulent Reynolds number are shown in Figure 2-1. Constant Damkohler numbers D_a^{fl} correspond to lines of slope ½ in a log-log (D_a, Re_t) diagram. If $D_a^{fl} \geq D_a^{LFA}$,

the flame is expected to have a laminar flame structure because of sufficiently fast chemistry. If $D_a^{fl} \leq D_a^{LFA}$, extinction occurs because of large chemical time scales.

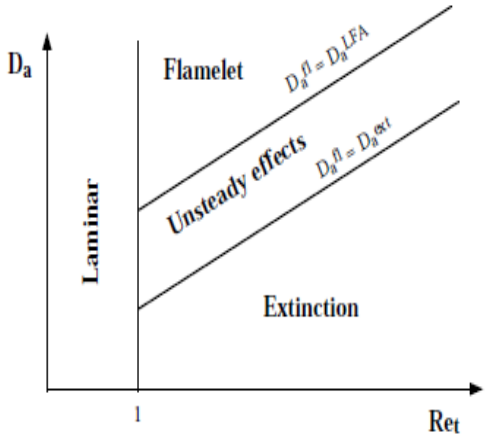

Figure 2-1. Regimes for turbulent non premixed combustion as a function of Damkohler number and turbulent Reynolds number

2.2 Turbulent Combustion Theory

2.2.1 Interaction between Flames and Turbulence

Laminar concepts break down when flows entering a flame front are turbulent. Turbulence may be characterized by the fluctuations of all local properties and occurs for sufficiently large Reynolds number, depending on the system geometry. Any property 'f' is generally split into mean ($\bar{f}$) and fluctuating (f') contributions.

$$f = \bar{f} + f' \tag{2-1}$$

This averaging process is defined as an ensemble average which is the average of the realizations at the same instant of the same instant of the same flow field.

The turbulent strength is generally characterized by the turbulent intensity I, which is the ratio of the root mean square of the fluctuation f' and the mean value $\bar{f}$.

$$I = \frac{\sqrt{\overline{f'^2}}}{\bar{f}} \tag{2-2}$$

Turbulent fluctuations are associated with different scales ranging from the integral length scale l_t, to the smallest, Kolmogorov length scale η_k.

A Reynolds number is introduced with turbulence scale which is given by Equation 2-3, where $u'(r)$ is the characteristic mean velocity and v is the kinematic viscosity. For homogenous isotropic turbulence, the energy of the large scales flows to the smaller scales through Kolmogorov cascade.

$$Re(r) = {u'^2(r)r}/{\nu} \tag{2-3}$$

Dissipation ε is estimated as the ratio of the kinetic energy divided by the time scale.

$$\varepsilon = \frac{u'^2(r)}{r/u'(r)} = \frac{u'(r)^3}{r} \tag{2-4}$$

Kolmogorov scale η_k is controlled by viscosity and dissipation rate.

$$\eta_k = \left(\frac{\nu^3}{\varepsilon}\right)^{1/4} \tag{2-5}$$

The ratio of integral length scale l_t to Kolmogorov length scale η_k is expressed as shown in Equation 2-6.

$$\frac{u'^3(r)/\varepsilon}{(\nu^3/\varepsilon)^{1/4}} = \frac{\ell_t}{\eta_k} = Re_t^{3/4} \tag{2-6}$$

Flame strain $\kappa(r)$ measures the fractional rate of increase of the flame front area.

$$\kappa(r) = \frac{u'(r)}{r} = \left(\frac{\varepsilon}{r^2}\right)^{1/3} \tag{2-7}$$

Characteristic time scale of an eddy of size r is given by Equation 2-7.

$$\tau_m(r) = \left(\frac{r}{u'(r)}\right) = \left(\frac{r^2}{\varepsilon}\right)^{1/3} \tag{2-8}$$

The Kolmogorov and the integral length scales induce strain values given by

$$\kappa(r) = \sqrt{\frac{\varepsilon}{\nu}} \quad (2\text{-}9)$$

$$\kappa(l_t) = \frac{\varepsilon}{u'^2} \approx \frac{\varepsilon}{k} \quad (2\text{-}10)$$

2.2.2 Reynolds Average Navier Stokes (RANS) Simulation

RANS equations are the oldest approach to turbulence modeling and these techniques were developed to solve for the mean values of all quantities. An ensemble version of the governing equations is solved, which introduces new apparent stresses known as Reynolds stresses. This adds a second order tensor of unknowns for which various models can provide different closure levels. RANS models can be divided into two broad approaches.

2.2.2.1 Boussinesq hypothesis

This method involves using an algebraic equation for the Reynolds stresses which include determining the turbulent viscosity and solving transport equations for determining the turbulent kinetic energy and dissipation. Models include k-ε, mixing length and zero equation models.

2.2.2.2 Reynolds stress model

This approach attempts to solve the transport equations for the Reynolds stresses. This approach is computationally costly because of the introduction of several transport equations for all the Reynolds stresses.

2.2.3 Large Eddy Simulation (LES)

The main objective of this model is to explicitly compute the largest structures of the flow field which are generally larger than the grid size and model the small ones. This modeling technique had been widely used for non reacting flows as described by Ferziger [10] and Lesieur [11].

In LES, variables are filtered in spectral space or in physical space. The filtered quantity is defined as

$$\bar{f}(x) = \int f(x')F(x-x')dx' \tag{2-11}$$

Here F is the les filter. The filtered quantity $\bar{f}$ is resolved in the numerical simulation whereas f '=f-$\bar{f}$ corresponds to the unresolved part. Balance equations for LES are obtained by filtering the instantaneous balance equations. The filtered value of LES perturbation is not zero, i.e. $\bar{f}' \neq 0$ contrary to RANS averaging.

2.2.3.1 Filtered balance equations

The following equations are resulted by filtering the instantaneous balance equations.

$$\frac{\partial \bar{\rho}}{\partial t} + \frac{\partial}{\partial x_i}(\bar{\rho}\tilde{u}_i) = 0 \tag{2-12}$$

$$\frac{\partial \bar{\rho}\widetilde{u_i}}{\partial t} + \frac{\partial}{\partial x_i}\left(\bar{\rho}\widetilde{u_i}\tilde{u}_j\right) + \frac{\partial \bar{p}}{\partial x_j} = \frac{\partial}{\partial x_i}\left[\bar{\tau}_{ij} - \bar{\rho}(\widetilde{u_i u_j} - \widetilde{u_i}\tilde{u}_j)\right] \tag{2-13}$$

$$\frac{\partial(\bar{\rho}\tilde{Y}_k)}{\partial t} + \frac{\partial(\bar{\rho}\tilde{Y}_k\tilde{u}_i)}{\partial x_i} = \frac{\partial}{\partial x_i}\left[\overline{V_{k,i}Y_k} - \bar{\rho}(\widetilde{Y_k u_i} - \tilde{Y}_k\tilde{u}_i)\right] + \bar{\dot{\omega}}_k \quad k = 1, N \tag{2-14}$$

$$\frac{\partial \bar{\rho}\tilde{h}_s}{\partial t} + \frac{\partial}{\partial x_i}(\bar{\rho}ui\tilde{h}_s) = \overline{\frac{D\rho}{Dt}} + \frac{\partial}{\partial x_i}\left[\lambda\frac{\partial T}{\partial x_i} - \bar{\rho}(\widetilde{u_i h_s} - \widetilde{u_i}\widetilde{h_s})\right] + \overline{\tau_{ij}\frac{\partial u_i}{\partial x_j}} - \frac{\partial}{\partial x_i}\left(\overline{\rho\sum_{k=1}^{N} V_{k,i}Y_k h_{s,k}}\right) + \overline{\dot{\omega}_T} \tag{2-15}$$

In the Equations 2-12 to 2-15, the following quantities must be modeled.

1. Unresolved Reynolds stresses ($\widetilde{u_i u_j} - \widetilde{u_i}\widetilde{u_j}$), which require a subgrid-scale model.
2. Unresolved species fluxes ($\widetilde{u_i Y_k} - \widetilde{u_i}\widetilde{Y_k}$) and enthalpy fluxes ($\widetilde{u_i h_s}$ - $\widetilde{u_i}\widetilde{h_s}$).

3. Filtered laminar diffusion fluxes for species and enthalpy. These molecular fluxes can be modeled using a simple gradient assumption given by Equations 2.16 and 2.17.

4. Filtered chemical reaction rate ($\overline{\dot{\omega}_k}$).

$$\overline{V_{k,i}Y_k} = -\bar{\rho}\overline{D_k}\frac{\partial \widetilde{Y_k}}{\partial x_i} \tag{2.16}$$

$$\overline{\lambda\frac{\partial T}{\partial x_i}} = \bar{\lambda}\frac{\partial \tilde{T}}{\partial x_i} \tag{2.17}$$

Hence these filtered equations coupled to ad-hoc subgrid-scale models may be numerically solved to determine instantaneous filtered fields.

2.2.3.2 Smagorinsky model

The Smagorinsky subgrid-scale model is popular because of its simplicity in formulation. Unresolved momentum fluxes are expressed according to Boussinesq assumption.

$$\tau_{ij} - \frac{\delta_{ij}}{3}\tau_{kk} = -\nu_t\left(\frac{\partial \overline{u_i}}{\partial x_j} + \frac{\partial \overline{u_j}}{\partial x_i}\right) = -2\nu_t\overline{S_{ij}} \tag{2-18}$$

Here ν_t is a subgrid scale viscosity modeled from dimensional arguments as

$$\nu_t = {C_s}^2\Delta^{4/3}{l_t}^{2/3}|\bar{S}| \tag{2-19}$$

Here l_t is the turbulence integral length scale, C_s is a model constant, which typically varies from 0.1 to 0.2. In the above equation, $\bar{S}$ is the resolved shear stress.

The Equation 2-18 can be simplified assuming l_t is of the order of grid size to the Equation 2-19.

$$\nu_t = (C_s\Delta)^2|\bar{S}|. \tag{2-20}$$

Unresolved scalar fluxes are often described using a gradient assumption similar to Reynolds averaged Navier Stokes assumption.

$$\widetilde{u_i Y_k} - \tilde{u}_i \tilde{Y}_k = -\frac{\nu_t}{Sc_k}\frac{\partial \tilde{Y}_k}{\partial x_i} \quad (2\text{-}21)$$

Sc_k is a subgrid scale Schmidt number. The subgrid scale viscosity ν_t is estimated from unresolved Reynolds stresses model such as Smagorinsky model.

2.2.4 Detached Eddy Simulation (DES)

DES is a hybrid model that attempts to combine the best aspects of RANS and LES methodologies in a single solution strategy. This model treats the near wall regions in a RANS-like manner and the rest of the flow in LES-like manner. This model was originally formulated by replacing the distance function d in the Spalart-Allmaras model with a modified distance function $\check{d}$ (min [d, $C_{DES}\Delta$]), where C_{DES} is a constant and Δ is the largest dimension of the grid cell in question. The modified distance function causes the model to behave as a RANS model in regions close to the wall and in a Smagorinsky-like manner away from the walls. DES generates finer turbulent eddies than RANS and quantitative results are superior to those of RANS.

2.2.5 Governing Equations in the Standard k-ε Model

Two equation models are the simplest and complete turbulence models, where solution of two separate transport equations allows the turbulent velocity and length scales to be determined independently. A standard k-ε model falls in this category. This model assumes the flow to be fully turbulent and molecular viscosity effects are negligible in the derivation of the k-ε model.

The turbulent kinetic energy k and rate of dissipation ε are obtained from Equation 2-22 and Equation 2-23.

$$\frac{\partial}{\partial t}(\rho k) + \frac{\partial}{\partial x_i}(\rho k u_i) = \frac{\partial}{\partial x_j}\left[\left(\mu + \frac{\mu_t}{\sigma_k}\right)\frac{\partial k}{\partial x_j}\right] + G_k + G_b - \rho\epsilon - Y_M + S_k \quad (2\text{-}22)$$

$$\frac{\partial}{\partial t}(\rho \epsilon) + \frac{\partial}{\partial x_i}(\rho \epsilon u_i) = \frac{\partial}{\partial x_j}\left[\left(\mu + \frac{\mu_t}{\sigma_\epsilon}\right)\frac{\partial \epsilon}{\partial x_j}\right] + C_{1\epsilon}\frac{\epsilon}{k}(G_k + C_{3\epsilon}G_b) - C_{2\epsilon}\rho\frac{\epsilon^2}{k} + S_\epsilon \quad (2\text{-}23)$$

In Equations 2-22 and 2-23, $G_k$represents the generation of turbulent kinetic energy due to mean velocity gradients and $G_b$represents the generation of turbulent kinetic energy due to buoyancy. Y_M represents the contribution of the fluctuating dilatation in compressible turbulence due to overall dissipation rate. $C_{1\epsilon}$, $C_{2\epsilon}$, $C_{3\epsilon}$ are constants. σ_k and σ_ϵ are turbulent Prandtl numbers for k and ε. S_k and S_ϵ are user defined source terms. The turbulent viscosity is computed as shown in Equation 2-24.

$$\mu_t = \rho C_\mu \frac{k^2}{\epsilon} \quad (2\text{-}24)$$

The model constants $C_{1\epsilon}$, $C_{2\epsilon}$, C_μ, σ_k and σ_ϵ have the defaults values of 1.44, 1.92, 0.09, 1.0 and 1.3.

2.3 Plasma Assisted Combustion

Plasma based technologies have been developed to mainly improve ignition reliability, avoid flame instabilities and reduce emissions in a wide variety of applications, including aerospace propulsion systems, land based power generation units, incinerators, heaters, etc. Technologies in the field of plasma assisted combustion

can be divided into several groups such as plasma igniters, plasma pilots and flame sustainers, plasma fuel nozzles, spatial arc, fuel reformers and coal gasifiers, etc.

Plasma igniters are the most developed units for short term operations based on the thermal DC torches, RF and MW initiators [12] for sub- and supersonic flows. They normally replace spark plugs and have power consumption from 500W to 1 kW. The main advantage is higher plasma plume volume and velocity compared to a conventional spark plug, which allows deeper penetration of the high reactive plasma plume into the combustion zone for more reliable ignition.

Plasma fuel nozzle is a combination of plasma generator and fuel atomizer with simultaneous fuel atomizing, ignition and flame control. Several experimental nozzles for gaseous and liquid fuels with a flexi-fuel operation and steam feeding are under development.

Figure 2-2. Plasma igniter in operation [12]

The main advantages of these nozzles are increased ignition reliability, wider equivalence ratio range, reduction of combustion zone geometry, reduction of the

combustion walls temperature, increase in combustion efficiency and achieving smokeless operation.

Spatial Arc [13] is a non-thermal high voltage discharge source of ignition and flame control inside a combustion chamber. Employing the combustor walls as the electrodes, this arc with averaged power consumption from 10W to 1 kW provides simple and energy efficient solution for gas fired furnaces and combustors, particularly lean burned ones.

Sy Stange et al. [14] studied the effect of a dielectric barrier discharge applied to a fuel gas before it is mixed with air and is burned. Experiments indicate that this improves the flame stability and assists combustion in extreme lean-burn conditions. The improvement has been attributed to the capability of the plasma to break the fuel gas into smaller pieces, known as cracking, and creates reactive radicals.

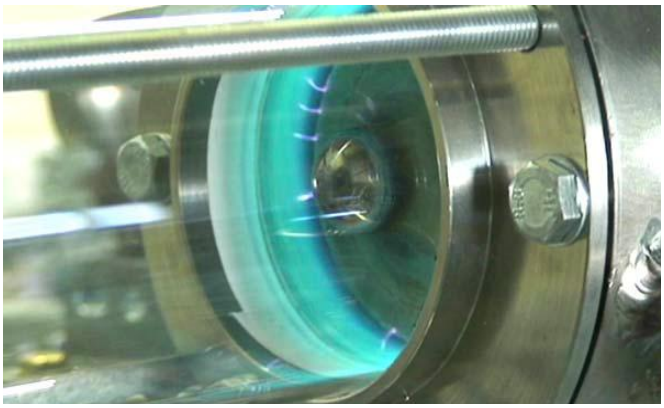

Figure 2-3. Reverse vortex combustor with 10W spatial arc [13]

A schematic of the vertical dielectric barrier discharge reactor is shown in Figure 2-4. The outer, high voltage electrode was a piece of copper mesh. An oscillating high voltage of 8-10 kV and frequency 425 Hz was applied to it. The mesh outer electrode surrounded a quartz tube with an inner diameter of 12.5 mm and a thickness of 3.175 mm. The inner electrode was a grounded stainless steel tube having an outer diameter

of 9.5 mm. The ends of the electrodes and the end of the quartz tube were separated by a 6 cm mixing region.

Figure 2-5 shows the effect of plasma on the flame. In the figure, in cases a and b, the flame propagates upward only, which indicates that the flame propagation rate is insufficient to overcome the upward flow of the propane-air mixture. When the plasma is applied, the flame begins to propagate downward and it becomes increasingly pronounced as the plasma power increases. The flame propagates more quickly because it is igniting and burning faster. This combustion enhancement may result from the improved cracking of propane, creation of reactive radicals or hydrogen generation.

Plasma-assisted chemical processes have been investigated by Toshiaki Yamato et al. [15], for the control of NO_x flue gas emissions. Non thermal plasma is able to oxidize NO to NO_2, but cannot convert NO_2 to N_2 effectively.

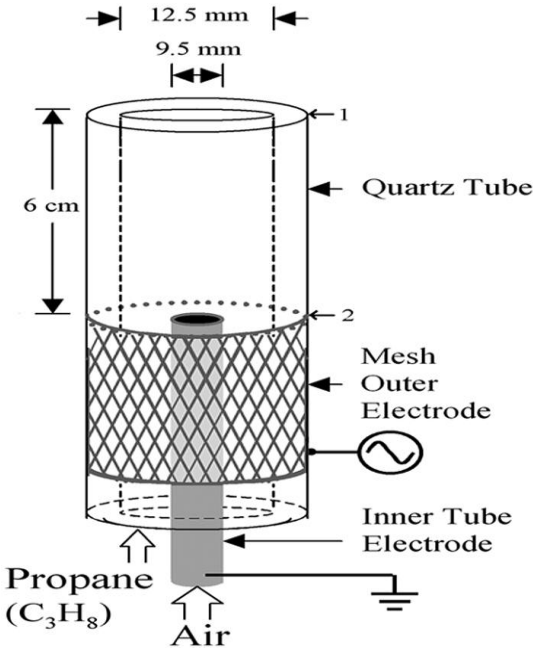

Figure 2-4. Coaxial dielectric barrier discharge reactor [14]

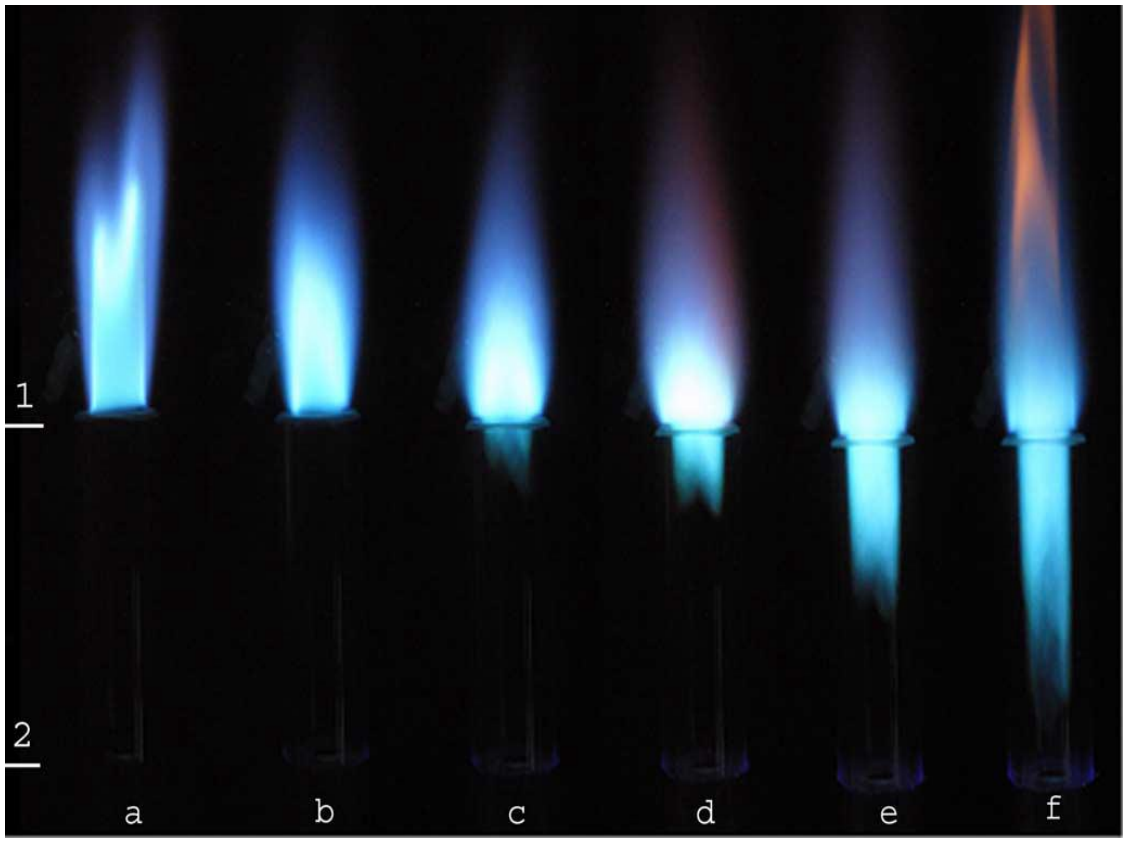

Figure 2-5. Combustion without plasma and increasing powers of plasma [14]

Hence, plasma-assisted chemical process was developed, where plasma reactor is employed to convert NO to NO_2 and the chemical reduction process to convert NO_2 to N_2, with minimum byproducts. This method was able to achieve nearly 100% NO_x decomposition with an extremely low power level (14 W/ ft^3/ min) and minimum N_2O formation. The above mentioned power consumption amounts to $ 299/ton of NO and the operating cost for the chemical reactor is $ 1448/ton. The total cost is $ 1747/ton, which is almost 20 times more economical compared to the conventional NO_x control techniques.

Figure 2-6 shows the variation of concentrations of NO, NO_2 and NO_x with applied voltage for a dielectric barrier ferroelectric packed-bed reactor (FPR) with an air flow rate of 2.0 L/min.

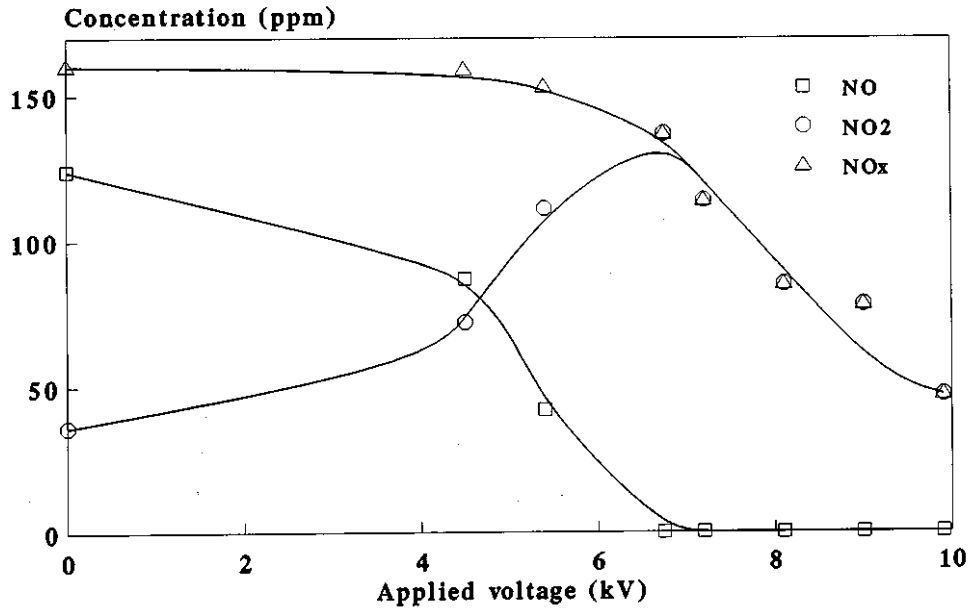

Figure 2-6. Variation of NO, NO_2, NO_x concentrations with applied voltage [15]

Plasma can initiate and accelerate combustion in engines and turbines. Plasma is a partially ionized gas, i.e. the electrons of certain molecules have been ejected and its function is to improve combustion. The plasma makes the fuel more reactive, which means that the engines can be run at speeds at which they are usually unstable. The plasma facilitates the fuel ignition, accelerates the combustion, prevents surges and hunting and improves the combustion homogeneity. It works as a combustion catalyst and possible applications include the use of lean fuel mixtures in order to reduce the emission of pollutants (particularly NO_x), the running of micro turbines and the improvement of supersonic combustion. When the electrodes are placed at the nozzle of the injector, the discharge comes into contact with the base of the flame and the plasma electrons collide with the molecules of air or fuel and form very reactive species, which triggers and accelerates the combustion. This effect is achieved with low power discharges, i.e. satisfactory effects are obtained with 10 to 20 watts of discharge for a flame whose combustion produces a power between 3000 to 5000 watts.

2.4 Plasma Theory

2.4.1 Electric Circuit

An electric circuit has been utilized by Roy et al. [1] to generate plasma. A Corona Magnetics Inc. high voltage transformer was used to generate the required high voltages in order to ignite the plasma discharge. A 10 kHz, sinusoidal waveform was first produced using a Tektronix arbitrary waveform generator (AFG3022B) and the waveform was further amplified using a QSC audio amplifier (RMX 2450). A circuit diagram is shown in Figure 2-7.

2.4.2 Force Approximation for Plasma Actuator

Singh and Roy [16] studied a plasma actuator using a self-consistent multibody system of quiescent air, plasma, and dielectric. Equations governing the motion of charged and neutral species have been solved with Poisson's equation. Based on first principle analysis, they approximated a functional relationship between electrodynamic force and physical and electrical control parameters and tested them numerically for air.

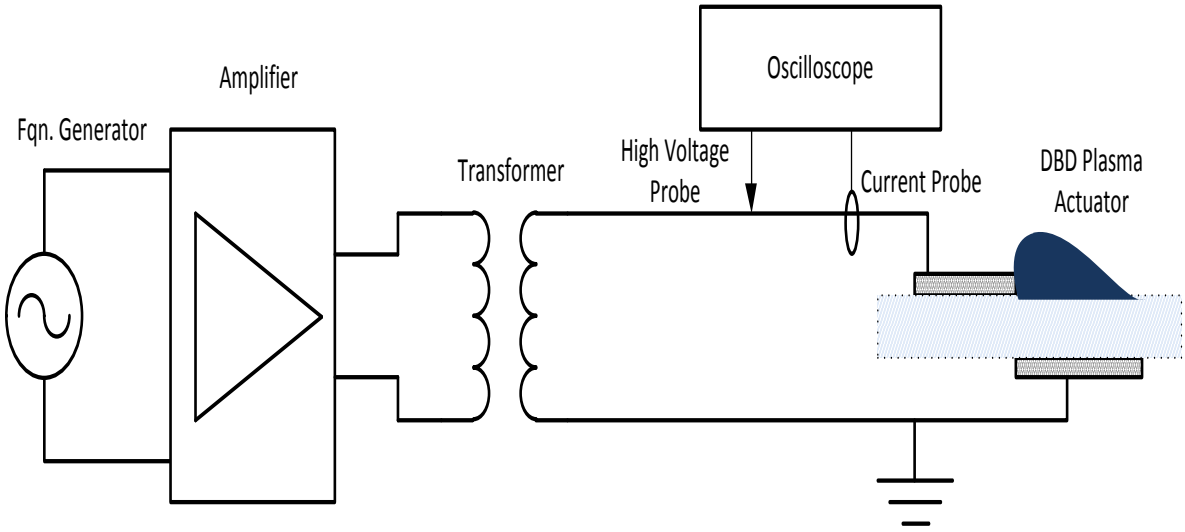

Figure 2-7. Electric circuit diagram [1]

2.4.2.1 Geometry description

Figure 2-8 shows simulation region with a length of 3cm and a height of 5 mm. The figure shows two electrodes separated by a dielectric. The lower part of the domain consists of a 1mm thick insulator with a dielectric constant $\varepsilon_r = 10$ and the upper part is filled with air of relative dielectric constant $\varepsilon_r = 1.0055$.

The powered electrode is located at y=1 mm and extends from x = 1.2 to 1.4 cm and the grounded electrode is at y=0 mm and extends from 1.6 to 1.8 mm. The rf and the grounded electrode are separated by a distance of 2 mm along the x axis. An alternating voltage of $\emptyset = \emptyset_O \sin(2\pi ft)$ is applied to the exposed electrode in volts. Different cases have been studied with applied rf potential $\emptyset_O$ = 800, 1000 and 1200 and the frequencies of rf potential f = 2.5, 5 and 10 kHz.

2.4.2.2 Numerical details

All the initial particle concentrations, except those of the electrons and nitrogen and oxygen molecules were assumed to be zero. Zero initial velocities have been chosen. Nitrogen and oxygen gas molecules were assumed to have an atmospheric ratio of 3.6. Initial oxygen molecule density was taken as $10^{26}/m^3$ and electron density as $10^9/m^3$. Time step was chosen adaptive in the process of solving the governing equations for densities and velocities of ion, electron, neutral species of N_2 and O_2 and electric potential. The electrodynamic force was approximated by Equation 2-25.

$$F = F_{x0}\phi_0^4 \exp\left(-\left\{\frac{[x-x_0-(y-y_0)]}{y}\right\}^2 - \beta_x(y-y_0)^2\right)\hat{\imath} + F_{y0}\phi_0^4 \exp\left\{-\left[\frac{x-x_0}{y}\right]^2 - \beta_y(y-y_0)^2\right\}\hat{\jmath} \quad (2\text{-}25)$$

F_{x0} and F_{y0} were taken from the average electrodynamic force obtained by solving air-plasma equations. As shown in Figure 2-2, x_0 is the midpoint between rf and the grounded electrode and y_0 is at the dielectric surface. The β_x and β_y values are functions

of dielectric material adjusted to match the velocity induced by the electrodynamic force. Different cases had been studied using F_{x0} = 2.6, F_{y0} = 2.0, $\beta_x = 8x10^5$, $\beta_y = 10^7$, x_0 = 0.015m and y_0 = 0.001m. There was a good agreement between solutions obtained by solving air-plasma equations and the approximated force.

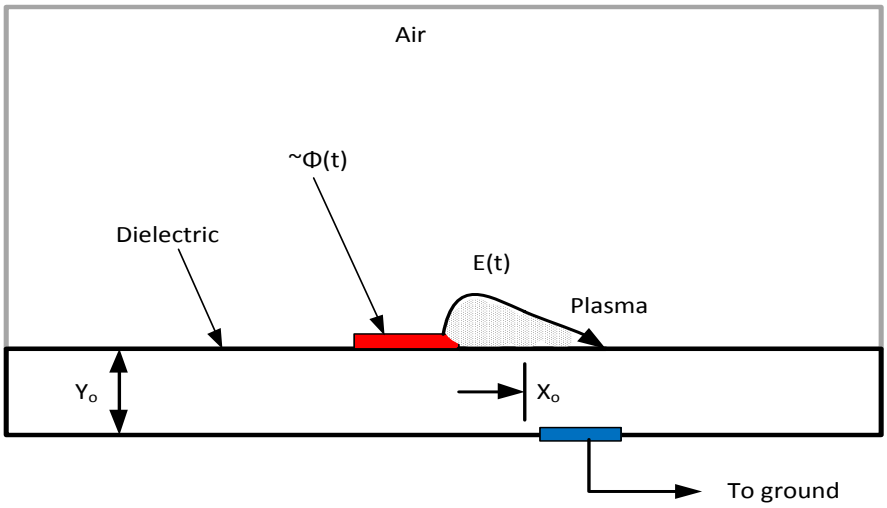

Figure 2-8. Geometry description of plasma actuator [16]

CHAPTER 3
COMPUTATIONAL MODEL

3.1 Description of Combustion Chamber Geometry

A methane fuelled coaxial jet combustor which has been discussed by C. D. Pierce et al. [17] is chosen for the numerical simulation. The geometry and the boundary conditions are chosen to yield complex flow pattern resembling those in a gas turbine combustor. There is a relatively large-diameter, low-velocity central fuel port surrounded by an annulus for the inlet of higher velocity, non-swirling air. A schematic of the coaxial jet combustor is shown in Figure 3-1.

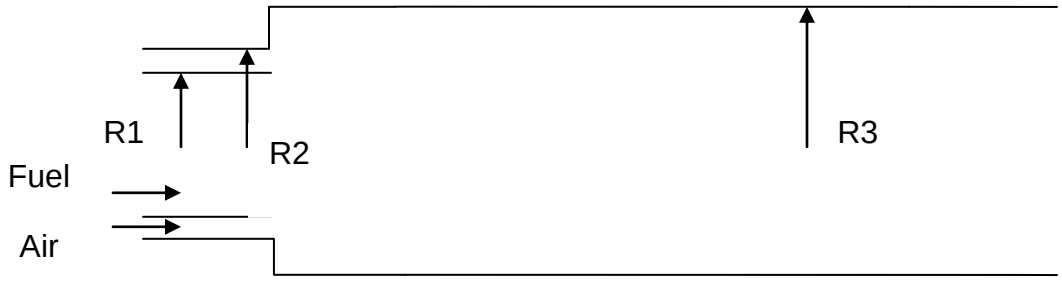

Figure 3-1. Schematic of the combustor [17]

The geometric dimensions and the flow conditions are listed in Table 3-1 along with units.

Table 3-1. Dimensions and the flow conditions [17]

Central pipe radius (R1) :	3.157 cm
Annular outer radius (R2)	4.685 cm
Combustor Radius (R3)	6.115 cm
Combustor length	100.0 cm
Mass flow rate of air	0.137 kg s^{-1}
Mass flow rate of fuel	0.0072 kg s^{-1}
Temperature of fuel	300 K
Temperature of air	750 K
Combustor pressure	3.8 atm
Equivalence Ratio	0.9
Bulk velocity of air at inlet	20.63 ms^{-1}
Bulk velocity of fuel at inlet	0.9287 ms^{-1}

3.2 Computational Model of Combustion Chamber

The present work has been employed in a commercially available CFD package known as Fluent. It has an advanced solver technology which provides fast and accurate results, flexible moving and deforming meshes and superior parallel scalability. New user models and extensive customization of an existing one has been made possible by allowing user defined functions. Moreover, one can easily pause a calculation, examine results with post processing, change any setting and continue the calculation again within a single application. This software has a wide application in turbo-machinery industry to analyze the flows in compressor, turbines, pumps, nozzles, ducts, etc. The solver for fluid in Fluent allows solving for incompressible / compressible, steady / transient, laminar / turbulent fluid flow in complex geometries.

3.3 Advantages of Carrying Out CFD Analysis

3.3.1 Speed

The speed with which a problem can be solved computationally is highly remarkable compared to an experimental investigation. Implications of different cases can be easily performed by a designer computationally leading to an optimum design. Application of the same experimentally can take longer amounts of time.

3.3.2 Detailed Information

A computer solution yields a complete and a detailed solution. It can provide the required variables such as velocity, pressure, density, temperature, concentration, etc. This allows a better understanding of the flow phenomenon in the regime.

3.3.3 Reduction of Experimental Risks

Experiments posing a safety risk which include pollutant formation and nuclear accidents can be replaced by computer simulations. This can reduce life threats and subsequent costs required for the equipment to meet the safety standards.

3.4 Steps for CFD Analysis

The steps involved in the present analysis are:

1. Creating and meshing the geometry.
2. Exporting the grid to CFD software.
3. Selection of solver, solver parameters and convergence criterion.
4. Specification of boundary conditions and initial condition.
5. Post processing and analysis of results.

3.5 Grid Generation

The generation of the grid including the modeling of geometry has been done in Gambit. It is a successful software for the construction of high quality computational meshes in two and three dimensional geometries. Features such as meshing capabilities for boundary layers and adapting the mesh based on the solution gradient yield high levels of accuracy in complex geometries.

3.6 Meshing Procedure

3.6.1 Creation of Coordinates

Coordinates in Gambit can be created by specifying the x, y, z locations of each coordinate.

3.6.2 Construction of Edges

In Gambit, the coordinates can be joined using a straight line or smooth curves such as conics, nurbs, etc. In the present study we use lines to connect the points. In general, it is advisable to create the edges in a systematic order, to avoid creation of inappropriate edges. The edge created is highlighted in yellow.

3.6.3 Construction of Faces

The construction of faces can be performed by selecting appropriate edges forming an enclosed surface. This construction process can be hindered even if a single edge enclosing the face is not selected. Formation of the face can be confirmed by noticing a change in the color from yellow to blue.

3.6.4 Creation of Volumes

Volume generation can be generated in many different ways in Gambit. The most common procedures are sweeping a face along a direction, revolving a face about an axis or stitching the faces. Formation of a volume can be confirmed by noticing a change in color from blue to green.

3.6.5 Meshing

The partition of the flow domain into a large finite number of smaller elements is known as meshing. Various parameters such as pressure, velocity etc can be studied at each of those smaller elements. The degree of fineness in meshing depends on the geometry of the domain and flow specifications. A fine mesh provides a better scope to understand the physics of the problem since it gives more elements to study the variation in the parameters. A much finer mesh is computationally costly consuming a longer time to be solved completely. In Gambit, meshing can be done to edges, faces and volumes. An important feature in this software is size function tool, which allows varying the mesh density in space. Generally, a much higher density is expected near the walls, because of the formation of boundary layer and at locations, where there is sudden change in the geometry such as a step, etc.

In the present study, the edges (walls) are meshed initially using the size function. The walls are meshed in such a way that density of elements is higher at the region

where there is an expansion of flow. An incremental factor of 1.02 and 1.10 has been used for the large and small walls. The above size function tool has been utilized effectively to capture the physics occurring in the boundary layer close to the wall. The meshed combustion chamber is shown in Figure 3-2.

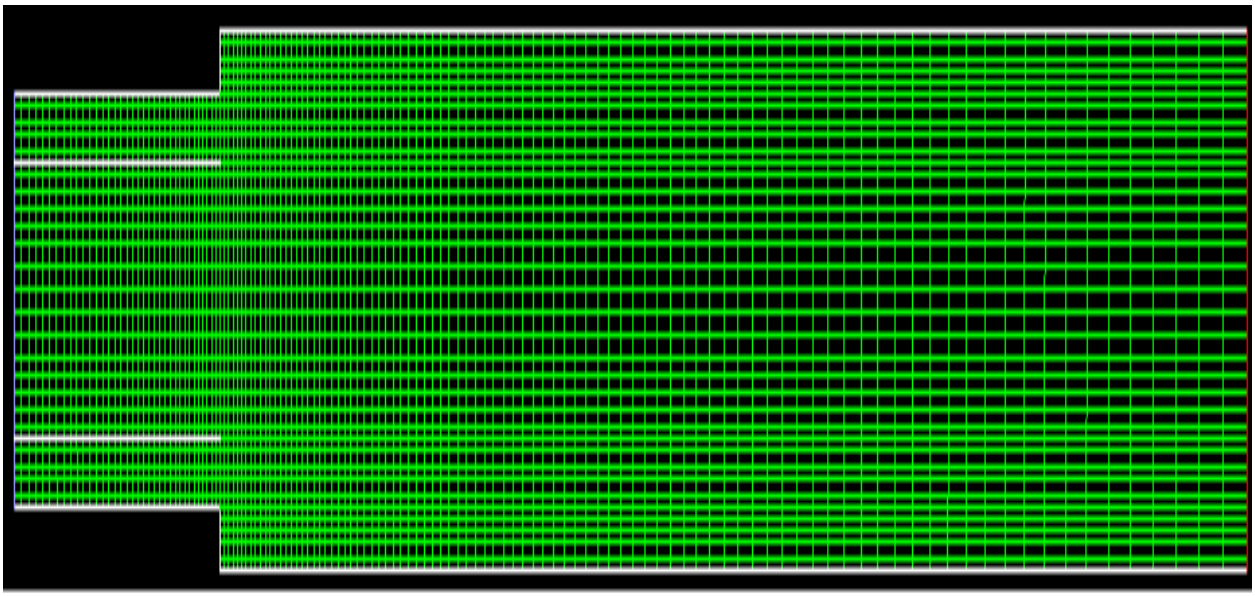

Figure 3-2. 2D mesh of the combustion chamber

Figure 3-2 shows the mesh over a complete domain of the chamber. For the visibility of the variation in grid sizes, a much coarser mesh has been shown. Figure 3-3 shows the mesh near the expansion of the flow and in this case a much denser mesh has been presented, which has been used for solving the problem.

The 2D mesh used for the present study contains a total of 37968 quadrilateral cells and 38636 nodes. Once the mesh is generated, the type of boundary condition associated with edge is applied. The boundary conditions used were velocity inlet, pressure outlet, wall and interior. Finally this mesh is exported in .msh format, which can be read by Fluent as a case file.

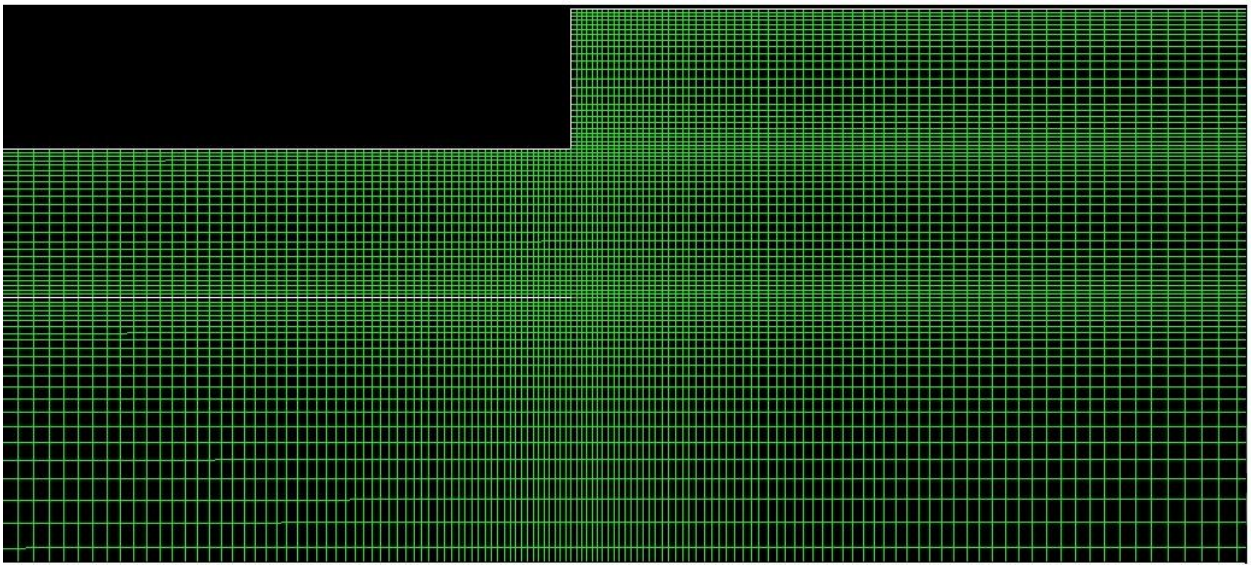

Figure 3-3. Zoomed view of the mesh of 2D combustion chamber

A three dimensional mesh with cylindrical geometry has also been created to solve the problem. The 3D mesh contains a total of 106992 cells and 113640 nodes. Figure 3-4 shows the 3D mesh.

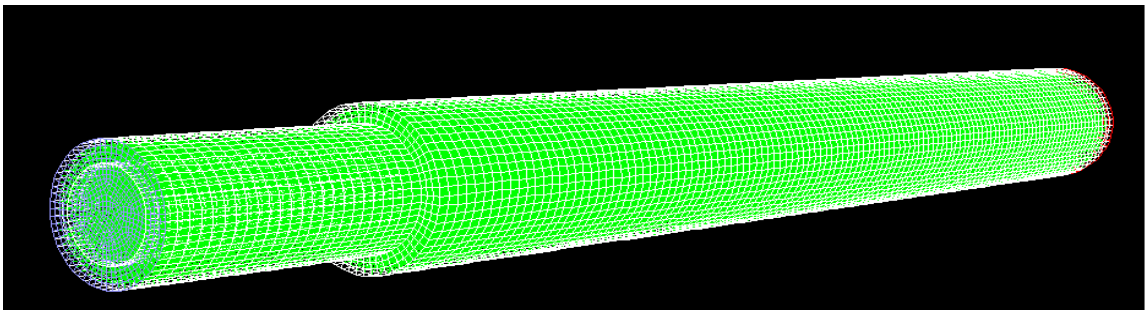

Figure 3-4. 3D mesh of the combustion chamber.

3.7 Solving

Solving is a crucial phase in CFD analysis. In the present study, solving has been performed in Fluent. The mesh is imported as a case file in Fluent. Grid should be checked so that the minimum volume is not negative. Information of the grid such as the number of cells, faces and nodes can be viewed.

3.7.1 Solvers

There are two different solvers in Fluent, the pressure based and the density based solver. The density based solver is generally used in flows with speeds greater than the sonic velocity. In the present study, the Mach number is low and hence pressure based solver has been chosen. An implicit formulation has been chosen for the problem, since it is much stable than the explicit solver. The solver can be chosen to be steady or unsteady depending on the problem specification. An absolute formation for velocity is employed to calculate the velocities at different nodes. Green-Gauss cell based model is chosen for the gradient option since a scalar gradient at the centroid of a given volume can be easily computed using the definition of derivatives. These schemes are chosen for ensuring stability, convergence and accuracy of the model. Figure 3-5 shows the modeling parameters for the solver.

3.7.2 Energy Equation

There is an option in Fluent to enable the energy equation. This equation is enabled when the energy equation needs to be solved. Practical example includes combustion. In the present study, the energy equation has been activated only while modeling combustion.

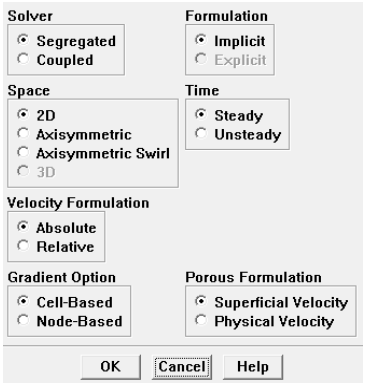

Figure 3-5. Solver parameters

3.7.3 Viscous Model

There are different viscous models such as inviscid, laminar, Spalart-Allmaras, k-epsilon, k-omega, Reynolds stress, detached eddy simulation and large eddy simulation. In 2D, large eddy simulation can be activated by typing the command (rpsetvar ‘les-2d? #t) in the command window. In the present study, a standard k-epsilon, large eddy simulation and detached eddy simulations models are used since the flow is turbulent. An enhanced wall treatment is chosen which includes pressure gradient effects and thermal effects in the case of combustion modeling. Figure 3-6 shows the modeling parameters for the viscous model.

3.7.4 Species Transport

In the present study, we are modeling combustion using methane-air mixture. Hence this mixture is chosen in the mixture materials. The volumetric option is turned on. The type of turbulence-chemistry interaction chosen is eddy-dissipation. Eddy-dissipation model is applicable only for turbulent flows and it computes only the mixing rate.

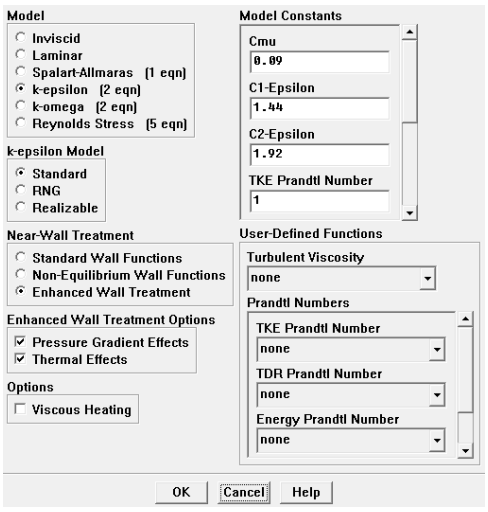

Figure 3-6. Viscous model parameters

3.7.5 Materials

The default material that is available in Fluent is air. In the present study, when combustion analysis is carried out, the materials that are considered are carbon dioxide, methane, oxygen, nitrogen and water. A piecewise polynomial approximation is considered for the specific heat C_P of all the materials. The density of air is made sure to be approximated as incompressible-ideal gas.

3.7.6 Boundary Conditions

In the present configuration, there is one fuel inlet, two air inlets and one outlet. The fuel and air inlets are specified as velocity inlets and the outlet as a pressure outlet. The bulk fuel velocity is 0.9287 m s^{-1} and the bulk air velocity is 20.63 m s^{-1}. The temperatures of air and methane are specified in the boundary conditions panel as 750 K and 300 K. The turbulence specification method is chosen to be intensity and hydraulic diameter. Generally, the value of turbulence intensity can be chosen from 5% to 10%. In the present study, a value of 10% has been chosen. The hydraulic diameter values for air and fuel inlets are 0.01528 m and 0.06314 m. Figure 3-7 shows the specification of fuel inlet conditions in the FLUENT panel. The wall temperatures are retained to a default value of 300 K.

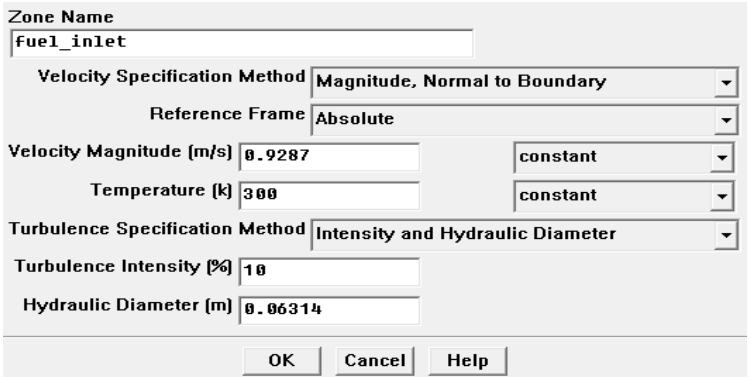

Figure 3-7. Fuel inlet specifications

A back pressure of 0 Pa and a back flow temperature of 300 K are chosen for the present study. The back flow hydraulic diameter is given a value of 0.1223. Figure 3-8 shows the pressure outlet specifications in the FLUENT panel.

3.7.7 User Defined Function

A user defined function (U.D.F) is a routine written in C language which can be dynamically linked with the solver. User defined functions are built since a standard interface cannot be programmed to anticipate all needs. A user defined function assigns values such as source terms to individual cells and cell faces in fluid and boundary zones. In the present study, plasma force is introduced in to the flow by applying body force source term to the cells using a user defined function. The plasma force is applied only after a particular time by incorporating time macros in the code.

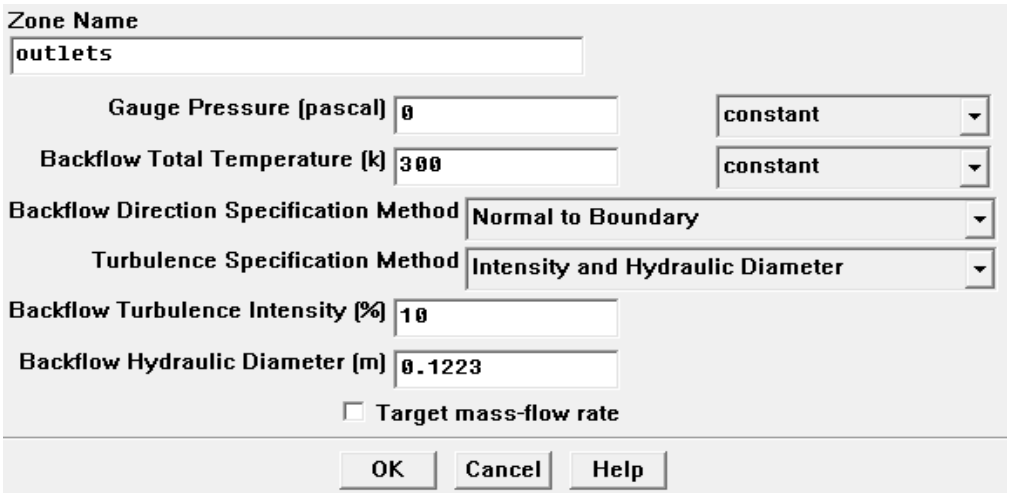

Figure 3-8. Pressure outlet specifications

The basic steps for using UDFs in Fluent are

1. Create a file containing the UDF source code.
2. Start the solver and read the case and data files.
3. Interpret or compile the UDF.
4. Assign the UDF to the appropriate zone in the boundary condition panel.
5. Set the UDF update frequency in the iterate panel.
6. Run the calculation.

3.7.8 Residuals

Residuals are the errors that are created in an iterative solution algorithm. These residuals under normal circumstances decrease as the solution progresses. On a computer with infinite precision, these residuals will go to zero as the solution converges. For Single precision computations, residuals can drop as many as six orders of magnitude before hitting round-off and double precision residuals can drop off to twelve orders of magnitude.

3.7.9 Convergence

A solution is said to be converged when the value no longer changes in the successive iteration. Convergence criteria can be tightened to obtain a more accurate solution. In the present simulation, a convergence criterion of 10^{-6} is employed for the residual of energy and criterion of 10^{-3} for the remaining residuals.

3.7.10 Discretization

Discretization is the process of replacing differential equations governing the fluid flow with algebraic equations solved at discrete points. In the present study, while performing a steady state simulation, a first order upwind scheme is used for momentum, turbulent kinetic energy and turbulent dissipation rate and energy discretizations. After the solution is converged, a second order upwind scheme is applied for the above mentioned discretizations to obtain a converged solution. In case of a 2D LES simulation, a bounded central difference scheme is employed for momentum, second order upwind scheme for energy and first order upwind scheme for the remaining discretizations. The same discretization schemes are employed in the case of a 3D DES simulation.

3.7.11 Initialization

Initialization is an important process in the computational analysis. In an iterative procedure, the fluid properties are updated based on the current solution. For the first iteration, the properties are updated based on the initialized solution. In the present case, the solution is initialized from all zones. The reference frame is chosen to be relative to the cell zone.

3.7.12 Iteration

In a steady state simulation, only the number of iterations is given as input to iterate. In a transient simulation, one has to input the values of the time step size and the number of time steps. The time step size can be chosen to be fixed or adaptive. Adaptive time stepping is available only in pressure based and density based implicit formulations. The automatic determination of the time step is based on the estimation of the truncation error associated with the time integration scheme. If the truncation error is less than a specified tolerance, the time step size is increased and decreased if the error is greater than the tolerance. Figure 3-9 shows the input data in the Fluent iterate panel for a LES simulation.

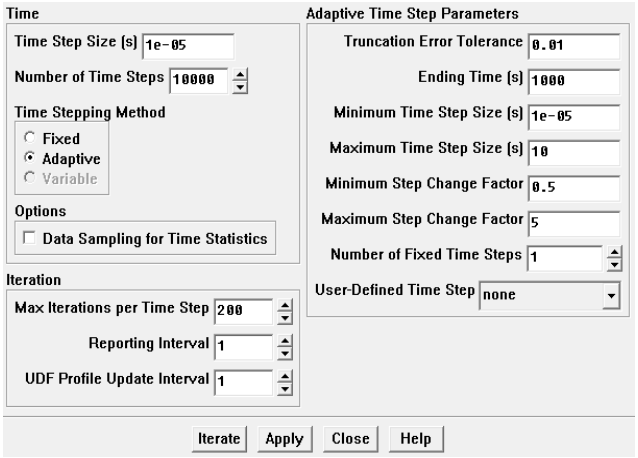

Figure 3-9. Iterate panel data

3.8 Grid Refinement Study

Examination of spatial convergence of a simulation is a method for determining the discretization error in a CFD simulation. The method involves performing the simulation on two or more successive finer grids. This method is known as the grid refinement study or grid convergence study. The order of the grid convergence involves the behavior of the solution error.

$$E = c\, h^{p} + H.O.T \qquad (3\text{-}1)$$

where c is a constant, h is a measure of grid spacing and p is the order of convergence.

A second order solution would have p=2. To assess the accuracy of the code and calculations, the grid should be sufficiently refined such that the solution is in the asymptotic range of convergence. Asymptotic range of convergence is obtained when the grid spacing is such that various grid spacings (h) and errors (E) result in the constancy of c, after neglecting the higher order terms.

3.9 Application of Plasma

Plasma actuator is attached to the combustor across the circumference at an axial location of z = 0.1m. The body force created has components in axial direction and outward radial direction. Figure 3-10 shows the region of application of plasma in the combustor. The red circle shows the location of the actuator across the circumference.

Figure 3-10. Region of application of plasma in the combustor.

CHAPTER 4
RESULTS AND DISCUSSIONS

The main aim of this study is to investigate the effect of plasma force on combustion phenomenon. Firstly, the effect of plasma force was studied on a non reacting flow and the fluid was chosen to be air. The effect of plasma force has been studied for different applied voltages across the electrode. Secondly, the effect was studied on a reacting flow where the fuel and oxidizer are chosen to be methane and oxygen. One of the important tasks was to successfully simulate the combustion process and obtain results, which are comparable to the discussed results in [17]. In the initial stages, two dimensional RANS and LES simulations have been performed. Since LES models turbulent eddies which are three dimensional in nature, the results obtained in 2D LES simulation are not physical in nature. Hence the 2D results have been restricted to those of RANS simulation. In the case of a 3D simulation, a steady state RANS solution has been chosen as an initial condition for the DES simulation. This simulation was run for a sufficiently long time, greater than the residence time. Later, plasma force was introduced into the domain employing a user defined function in FLUENT. Physically, a linear plasma actuator was attached to the combustor wall along the circumference of the chamber at a particular axial location (z = 0.1 m). Body force due to the generation of plasma, acts on the fluid layers underneath the wall up to a depth of 1cm, in the axial direction of the flow and outward radial direction. Results corresponding to each case are discussed in the later sections.

4.1 Non Reacting Flow

Initially, the effect of plasma force was studied on a single fluid, i.e. air. Air was introduced into a chamber with a velocity of 10 m/sec. Plasma actuators were attached

to the wall at two specific locations. The voltages applied across the electrode were chosen to be 20 kV, 25 kV and 35 kV respectively. The modification in the flow field with varied voltages is shown in the Figures 4-1 to 4-4.

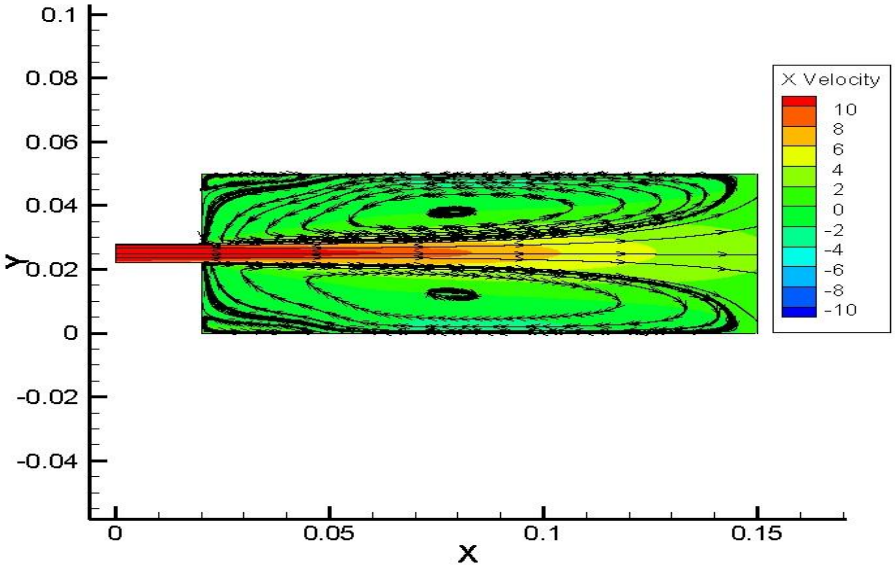

Figure 4-1. Velocity (m/s) contour plot without plasma force.

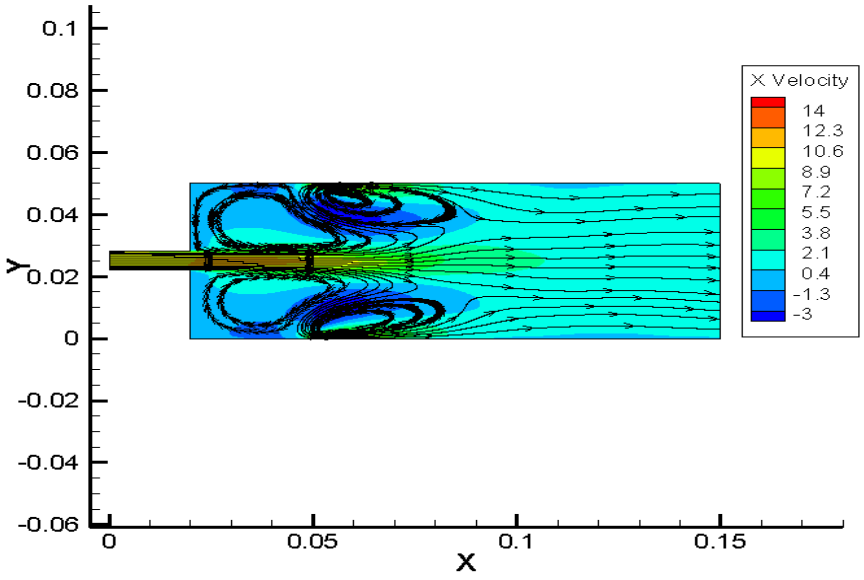

Figure 4-2. Velocity (m/s) contour applying a potential of 20kV across the electrodes.

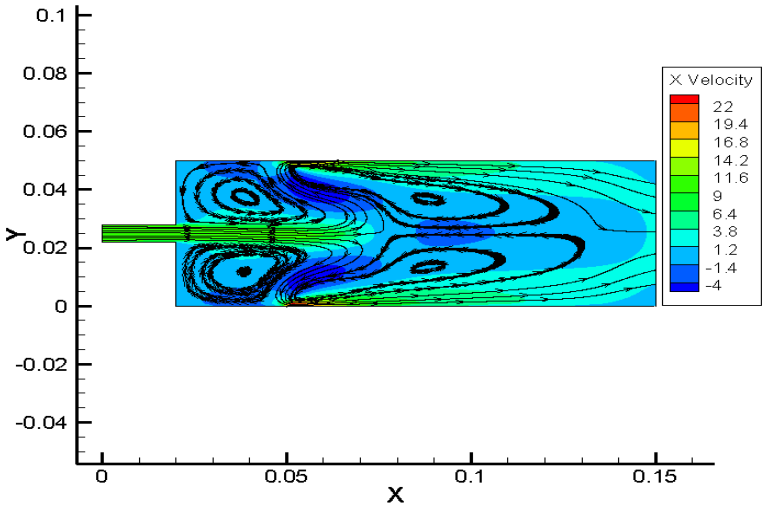

Figure 4-3. Velocity (m/s) contour applying a potential of 25 kV across the electrodes.

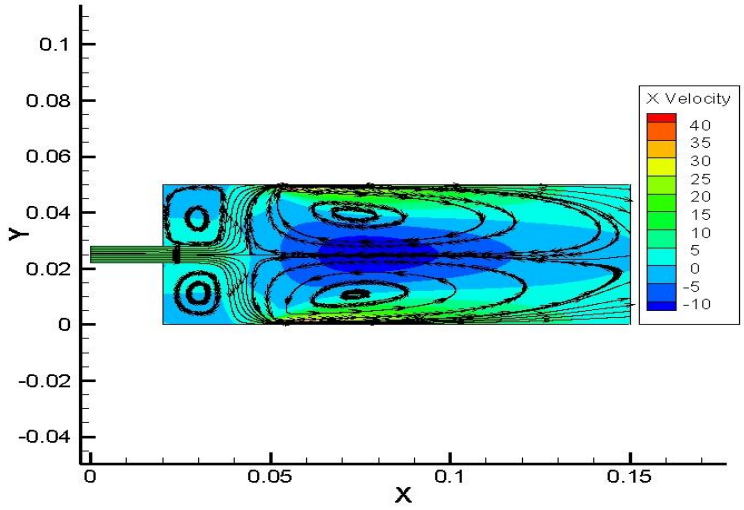

Figure 4-4. Velocity (m/s) contour applying a potential of 35kV across the electrodes.

In the initial case without any plasma force, there are two vortices stretching across the entire length of the chamber and two vortices of smaller length at the top and bottom left corner. When a plasma force is applied, a body force acts on the fluid in the positive x and positive y directions because of the top plasma actuator and in positive x and negative y directions because of the bottom plasma actuator. The magnitude of the

body increases as the voltage applied across the electrode increases and its effect on the modification of flow field is clearly visible from the Figures 4-1 to 4-4. When the plasma force is applied, the direction of the vortices is reversed and the magnitude of the clockwise vortex in the top half and the anticlockwise vortex in the bottom half increases with an increase in the plasma force.

4.2 2-D Steady State RANS Results

The present combustor configuration has been solved in a two-dimensional coordinate system. A RANS simulation has been performed on the present configuration until a converged solution has been obtained. The quality of the grid has been enhanced by employing size functions and density of the cells is higher near the walls and at the regions where there is a sudden change of geometry.

Steady state temperature contour, which is obtained after the solution has converged, has been shown in Figure 4-5. The temperature profiles are obtained assuming adiabatic walls and neglecting thermal radiation. The maximum temperature obtained is 2558 K and the temperature values are increasing along positive x direction.

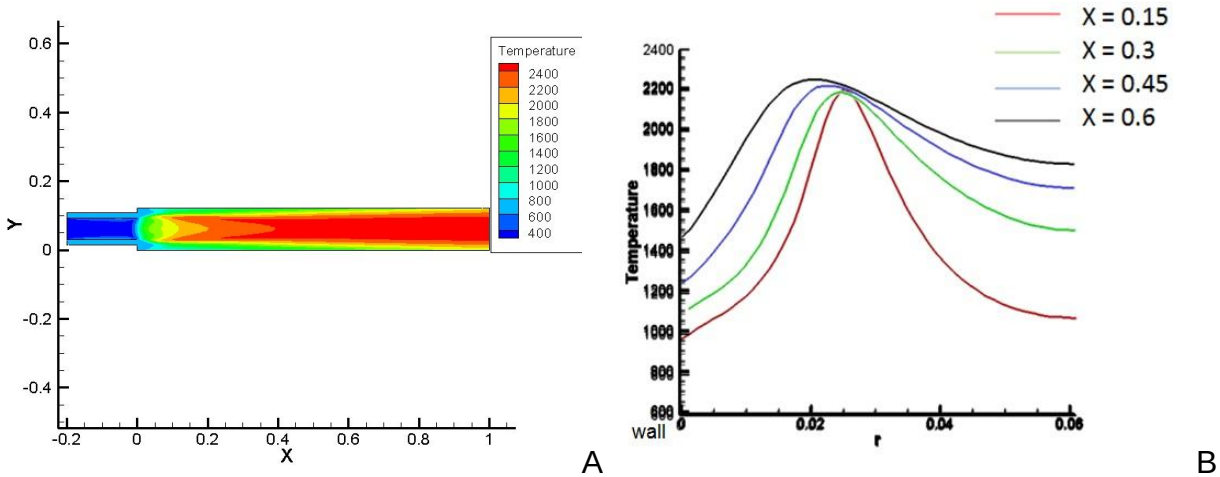

A B

Figure 4-5. 2D steady state temperature plots (K). A) contour plot, B) radial profiles at different axial locations.

Steady state x velocity contour, which is obtained after the solution has converged, is shown in Figure 4-6. Mass flow inlet condition has been specified in order to maintain an equivalence ratio of 0.9. Hence, the velocity values obtained are different from the actual experimental results. The maximum value of the velocity obtained is 2.86 m/sec.

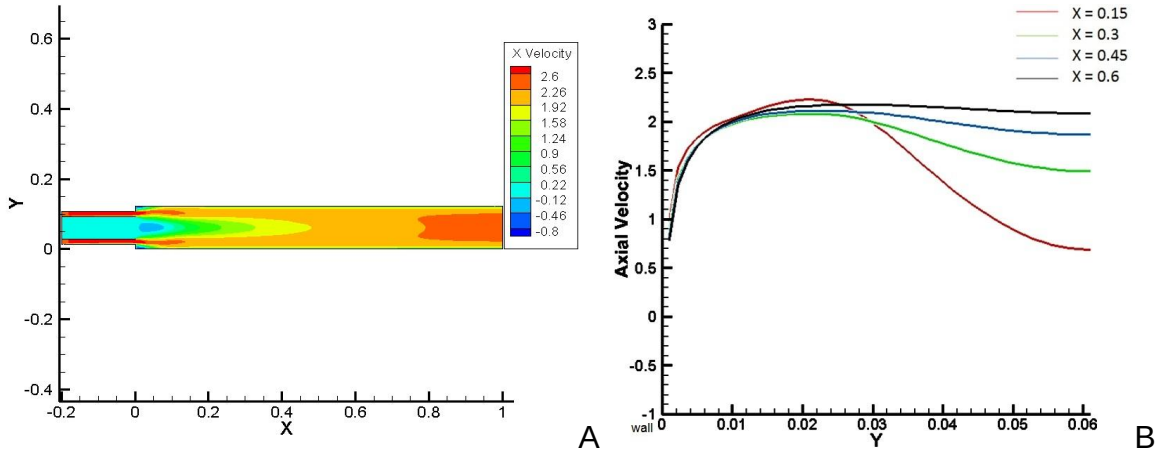

A B

Figure 4-6. 2D steady state axial velocity (m/s) plots. A) contour plot, B) radial profiles at different axial locations.

4.3 3D Steady State RANS Solution

The present configuration has been solved in three-dimensional coordinate system. RANS simulation has been performed on the present configuration until a converged solution has been obtained. Steady state contours of temperature, y-velocity, z-velocity, methane concentration and oxygen concentration are shown in the Figures 4-7 to 4-11. The contours are shown on a y-z plane. Figure 4-5 and Figure 4-7 show that the steady state temperature contours obtained in 2D and 3D simulations are same in magnitude. The contour plots reveal that after combustion, the temperature values are higher at the regions where there is less concentration of oxygen remaining. The z velocities obtained are comparable to the experimental data in [17].

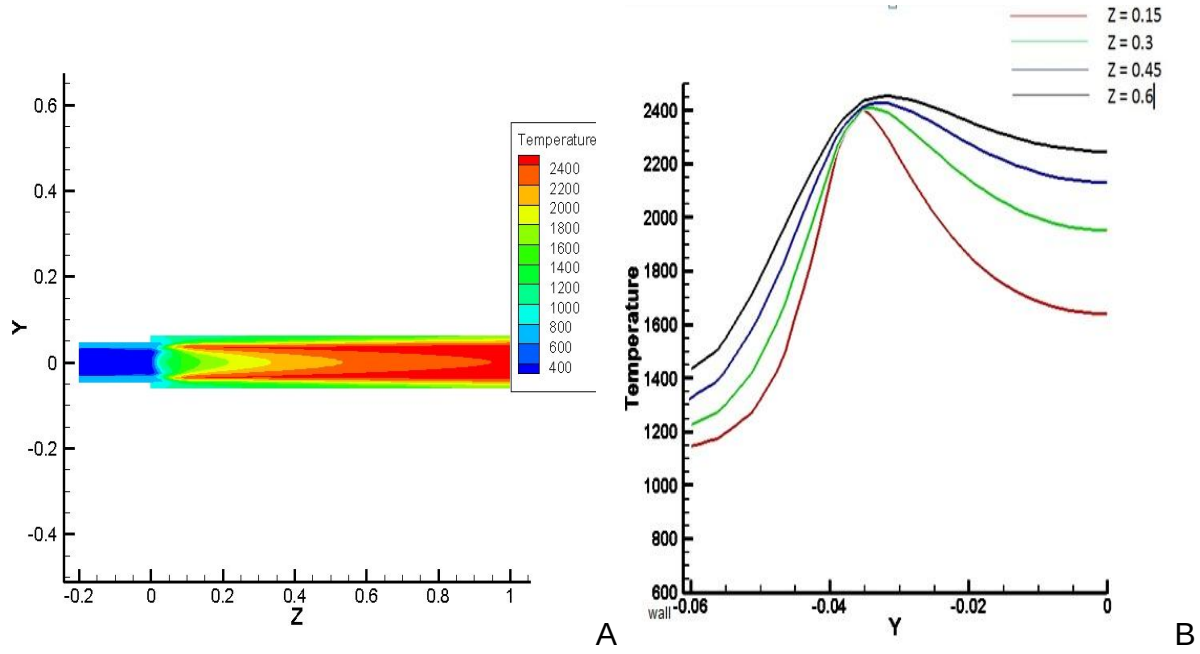

Figure 4-7. 3D steady state temperature (K) plots. A) contour plot, B) radial profiles at different axial locations.

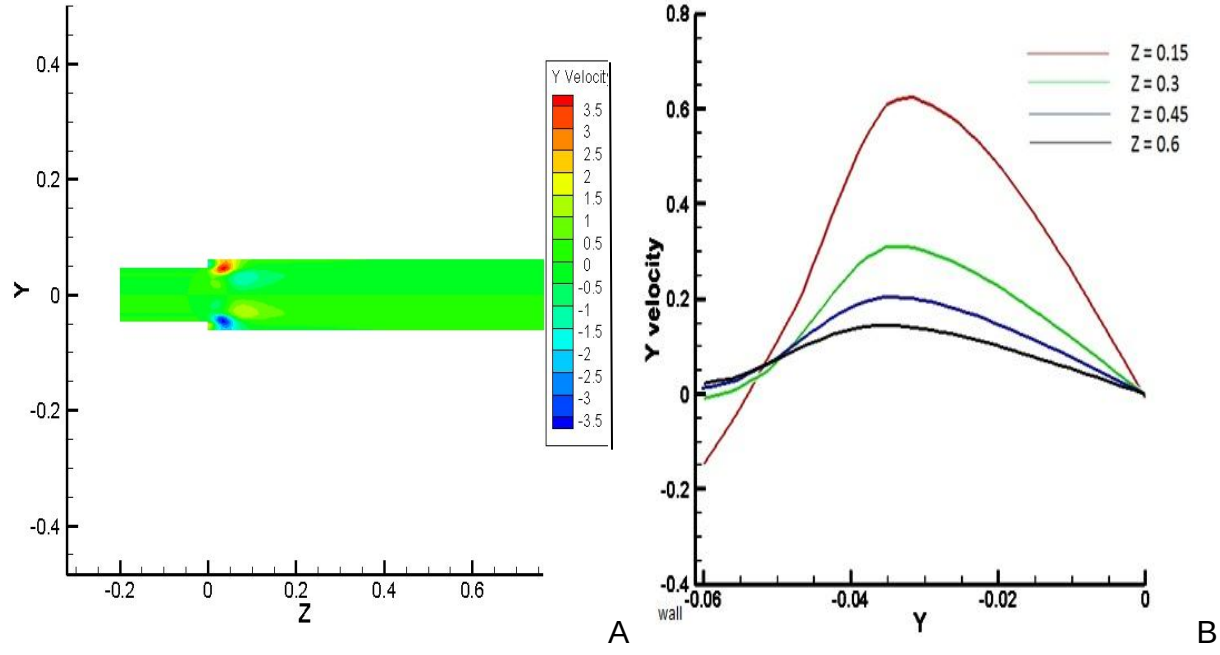

Figure 4-8. 3D steady state y velocity (m/s) plots. A) contour plot, B) radial profiles at different axial locations.

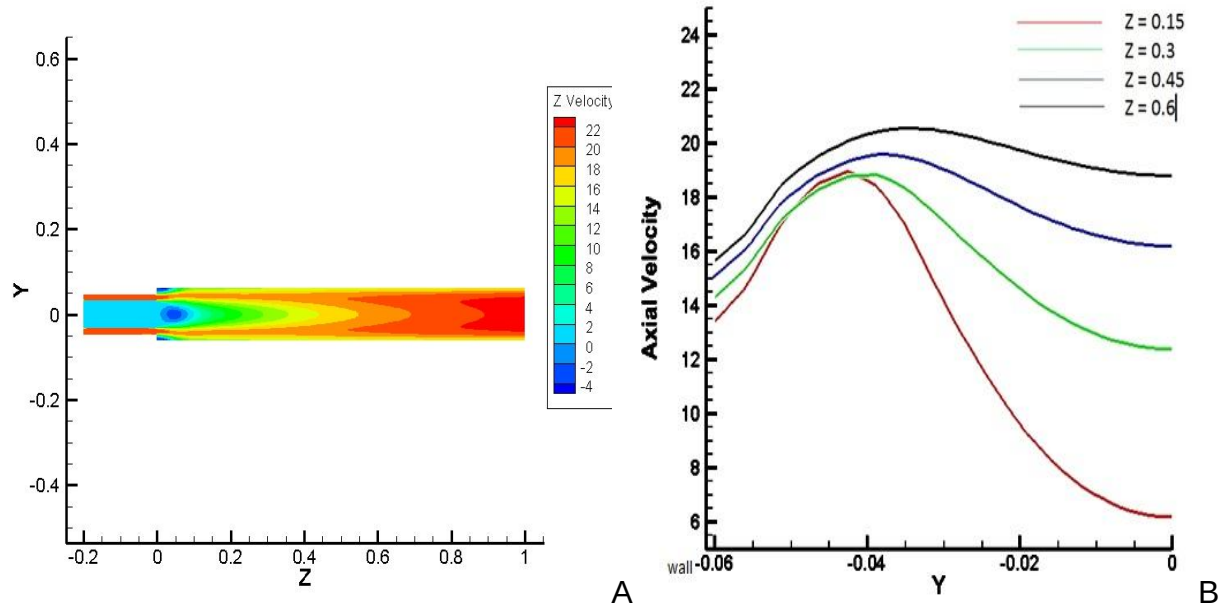

Figure 4-9. 3D steady state z velocity (m/s) plots. A) contour plot, B) radial profiles at different axial locations.

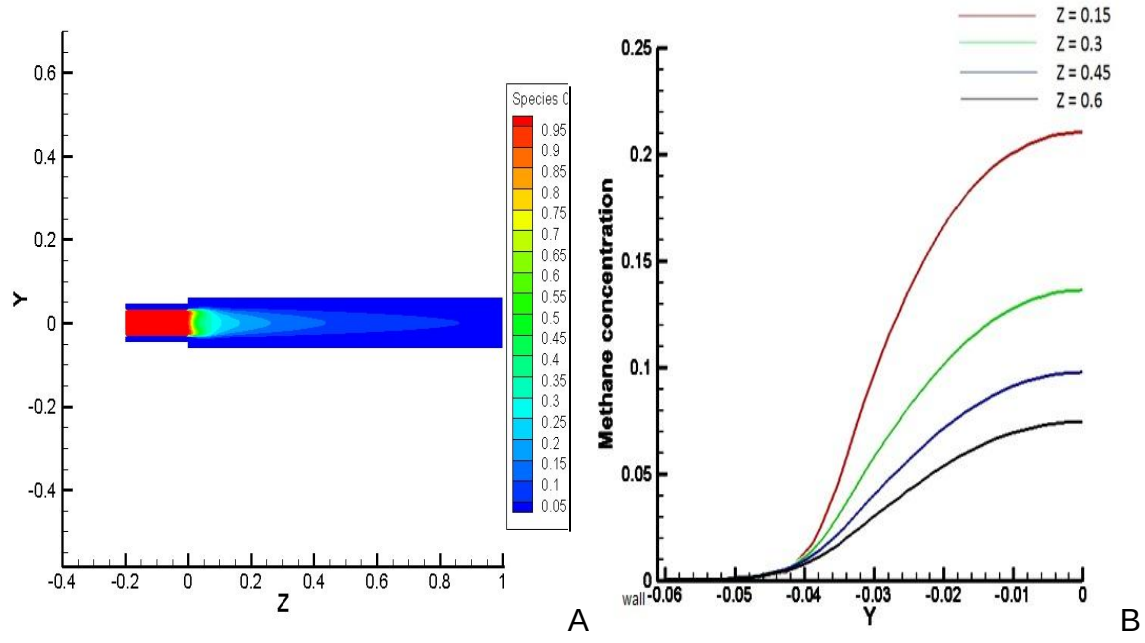

Figure 4-10. 3D steady state methane concentration plots. A) contour plot, B) radial profiles at different axial locations.

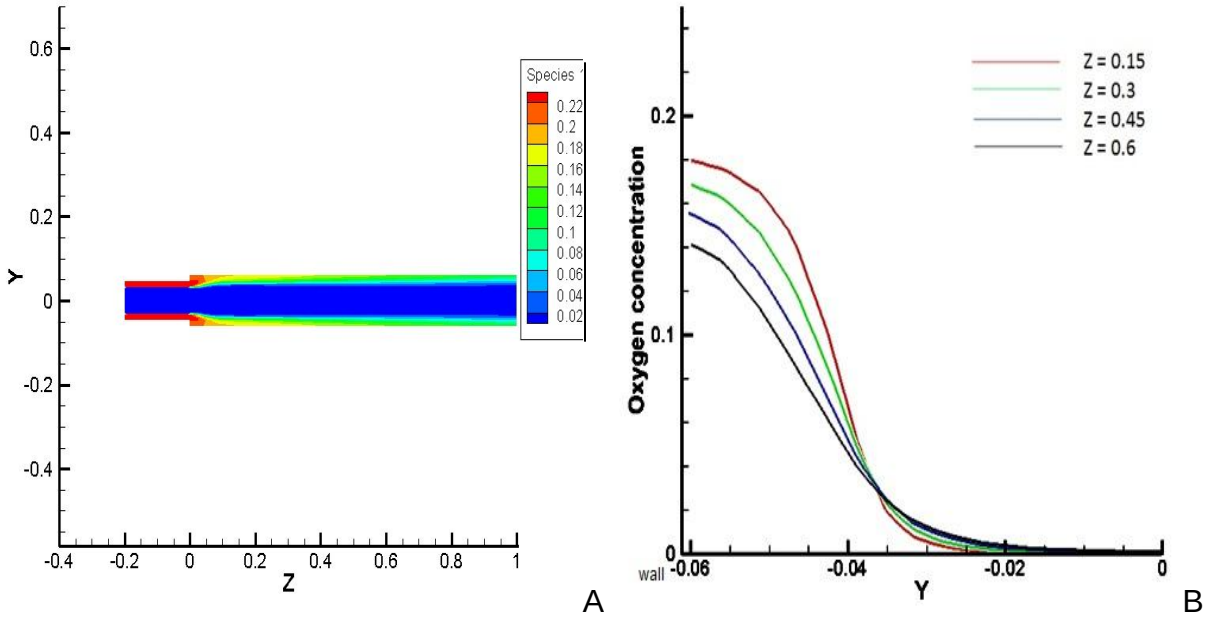

Figure 4-11. 3D steady state oxygen concentration plots. A) contour plot, B) radial profiles at different axial locations.

Figure 4-7 (B) shows the radial profiles of steady state temperature at different axial locations, z = 0.15, 0.3, 0.45 and 0.6 m. The peak temperatures are obtained at regions between the centerline and the wall because the recirculation region formed in front of the fuel port acts as a bluff body to the surrounding air stream. Increase in the peak values of the temperature is observed in the post recirculation regions. Figure 4-8 (B) shows the radial profiles of y velocity at different axial locations. The maximum velocity is decreasing in the positive axial direction since the flow is predominant in the axial direction. At z = 0.15 m, the magnitude of the maximum velocity is higher compared to the values at other axial locations because of the backward facing step in the flow domain, which deviates the flow in the direction towards the wall. Figure 4-9 (B) shows the radial profiles of axial velocity at different axial locations. At lower axial locations, the minimum of the axial velocity, which is near the centerline, is very low

compared to the values at other axial locations because of the recirculation region which re-circulates the combusted products towards negative axial direction. Figure 4-10 (B) shows the radial profiles of fuel (methane) concentration at different axial locations. The fuel concentration is maximum at the centerline region and decreases in the radial outward direction since it is injected through a central fuel port. The maximum value of the concentration is reducing in the positive axial location since the fuel is being combusted to form new products. Figure 4-11 (B) shows the radial profiles of oxygen concentration at different axial locations. The oxygen concentration is maximum at the walls and decreasing in the inward radial direction since oxygen is injected through an annular duct. The maximum value of the oxygen concentration is decreasing in the positive axial direction since oxygen is being consumed to form new products.

4.4 3D DES Results

A three dimensional unsteady simulation has been carried out employing the DES solver in FLUENT. The simulation has been run for sufficiently long time until there is no large change in the mean values. Radial profiles of the mean temperature and mean axial velocity at different axial locations are shown in the Figures 4-12 to 4-17. For DES results, z denotes the axial direction. The axial location distance has been normalized with R which has a value of 0.04685 cm. The computational domain discussed in [17] was limited to an axial distance of 8R, at which the convective outflow boundary conditions were specified. The radial mean temperature and the axial velocity profiles at the specified z locations are comparable to the profiles in [17]. Mean axial velocity has been normalized with the air velocity at the inlet, which is equal to 20.63 m/sec. The mean values of the temperature and z velocity at axial locations near the expansion

region are less than the peak temperature because of the presence of recirculation region.

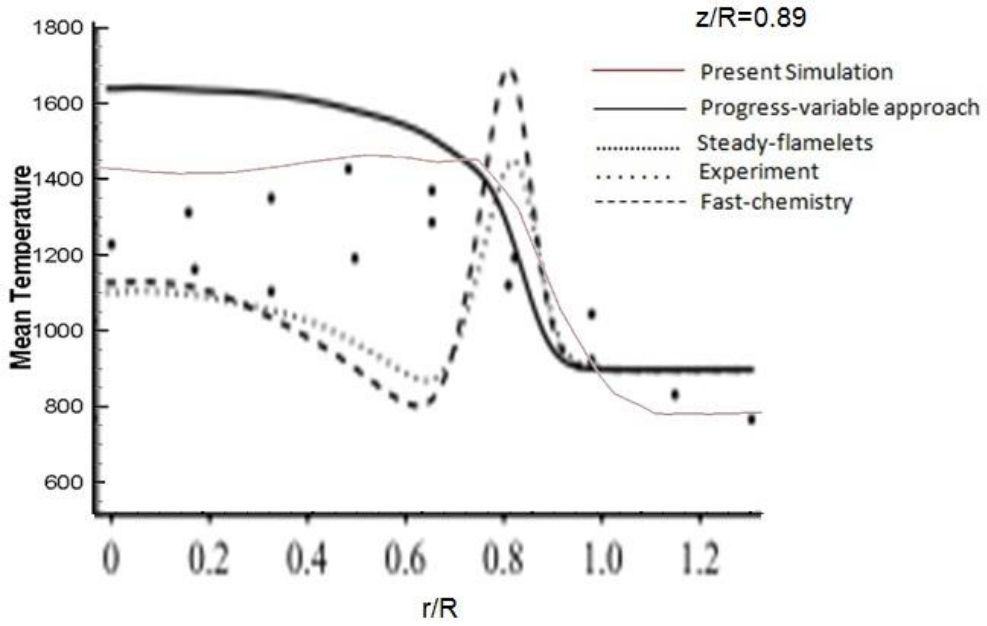

Figure 4-12. Radial profiles of mean temperature (K) at z/R = 0.89

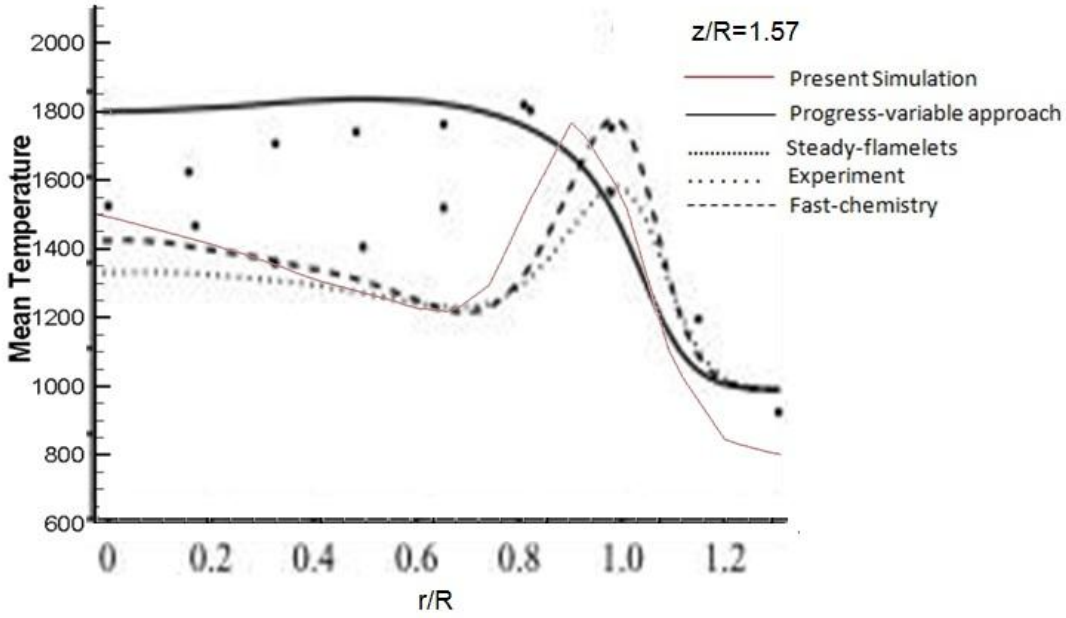

Figure 4-13. Radial profiles of mean temperature (K) at z/R = 1.57.

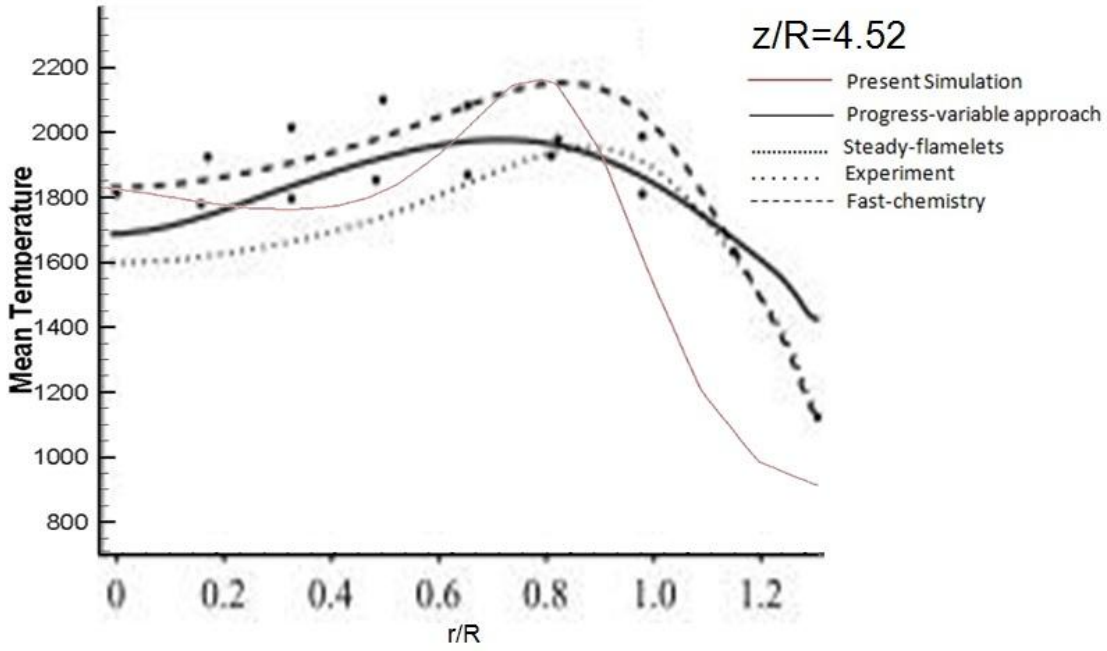

Figure 4-14. Radial profiles of mean temperature (K) at z/R = 4.52

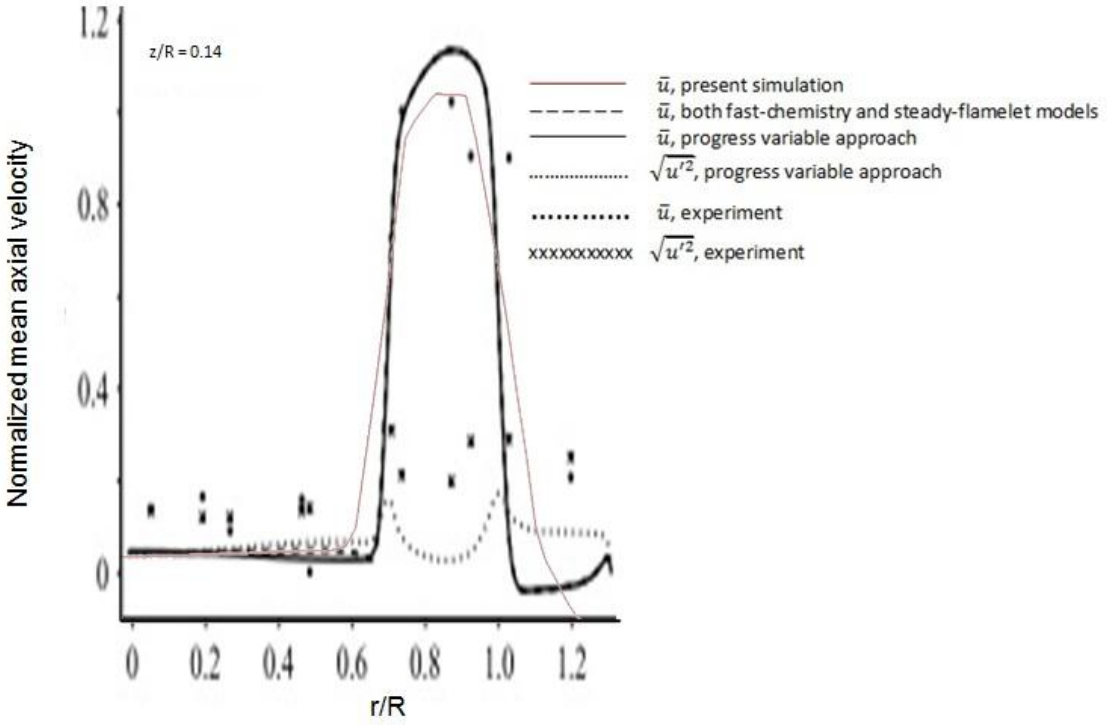

Figure 4-15. Radial profiles of mean axial velocity (m/s) at z/R = 0.14

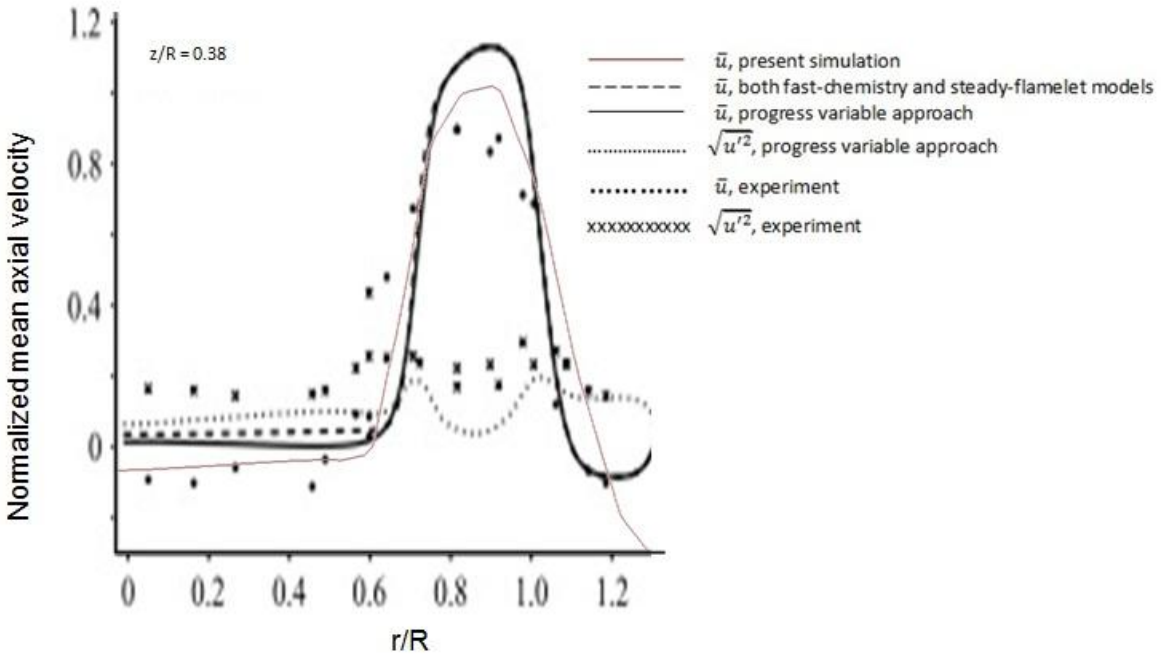

Figure 4-16. Radial profiles of mean axial velocity (m/s) at z/R = 0.38

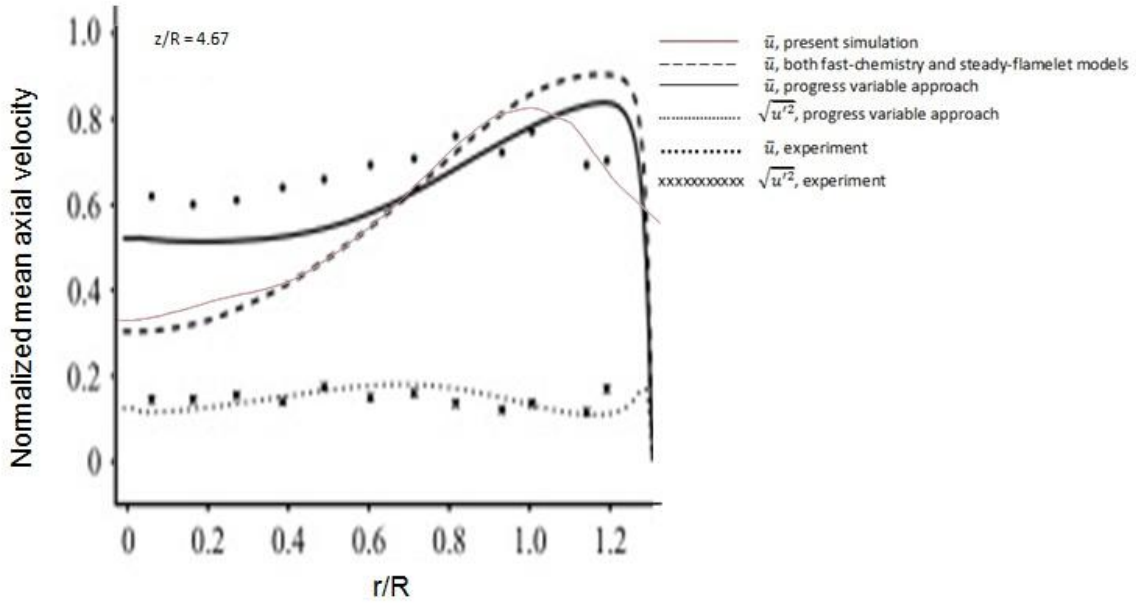

Figure 4-17. Radial profiles of mean axial velocity (m/s) at z/R = 4.67

The magnitude of the axial velocity increases from the center of the chamber and decreases in the direction of the wall. A no slip boundary condition is applied at the wall.

At locations corresponding to z/R = 0.14 and 0.38, the mean axial velocity profile is flatter near the center because of the presence of the recirculation region. Assuming adiabatic walls and negligible radiation, the temperature can be expected to behave very similar to the product mass fraction.

4.5 3D DES Results with Plasma Activation

DES simulation has been carried out without enabling the plasma actuators for a time of 0.075 seconds. Later, plasma force has been enabled and the simulation is allowed to run until the mean values remain unchanged. The flame structure has been modified because of the increase in the turbulence. Radial profiles of mean axial velocity and temperatures after applying plasma force are shown in the Figures 4-18 to 4-22. Mean axial velocity has been normalized with the air velocity at the inlet, which is equal to 20.63 m/sec.

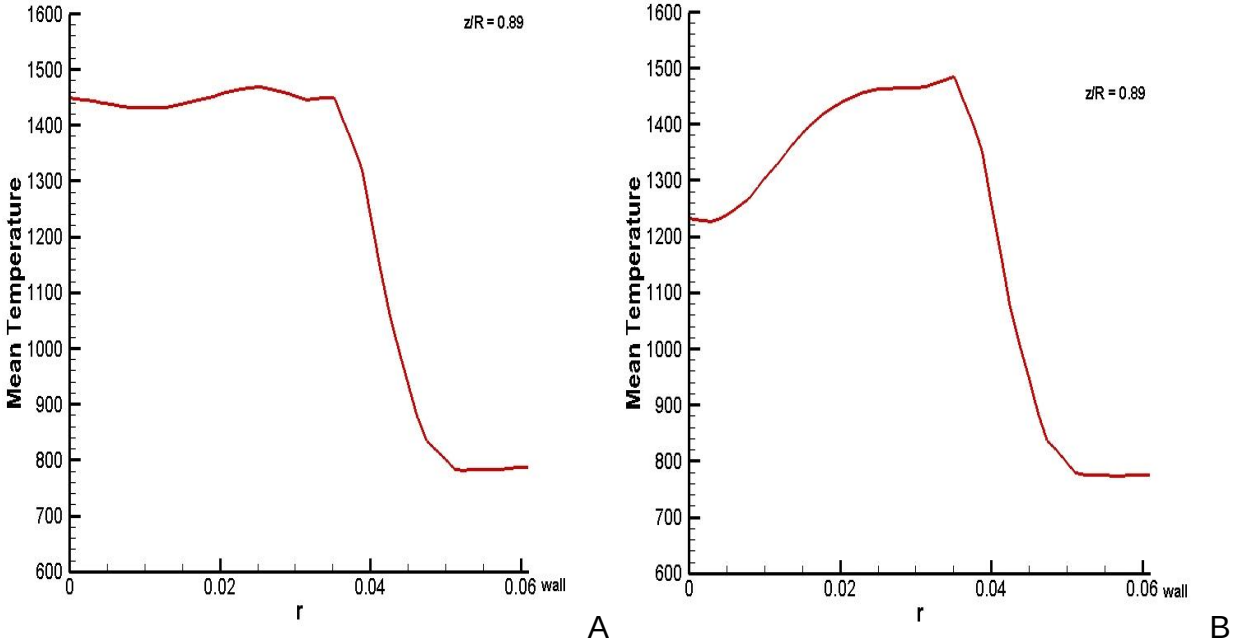

Figure 4-18. Radial profiles of mean axial temperature (K) at z/R = 0.89. A) without plasma, B) with plasma.

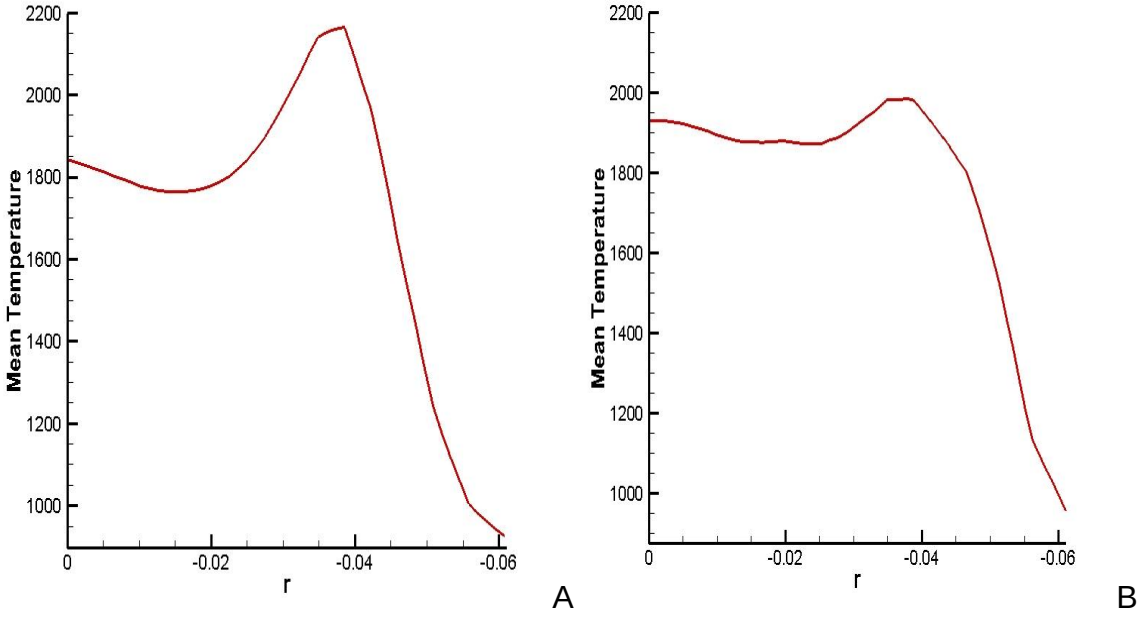

Figure 4-19. Radial profiles of mean axial temperature (K) at z/R = 4.52. A) without plasma, B) with plasma.

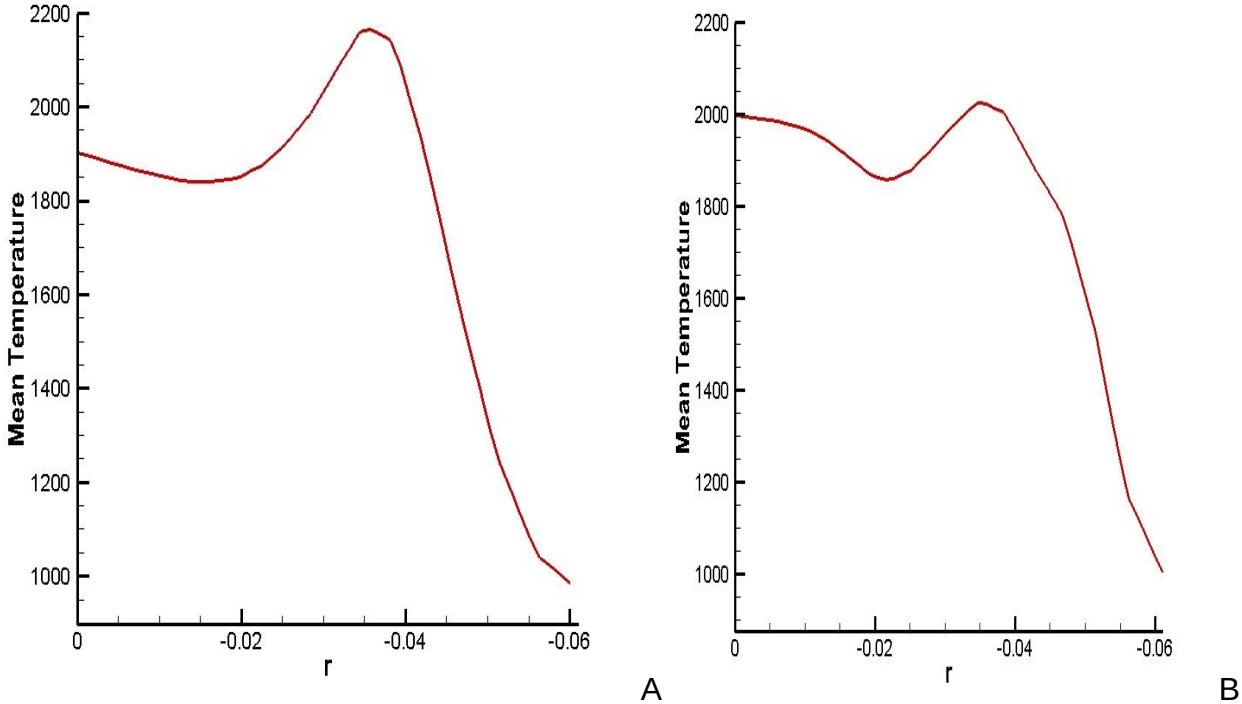

Figure 4-20. Radial profiles of mean axial temperature (K) at z/R = 5.20. A) without plasma, B) with plasma.

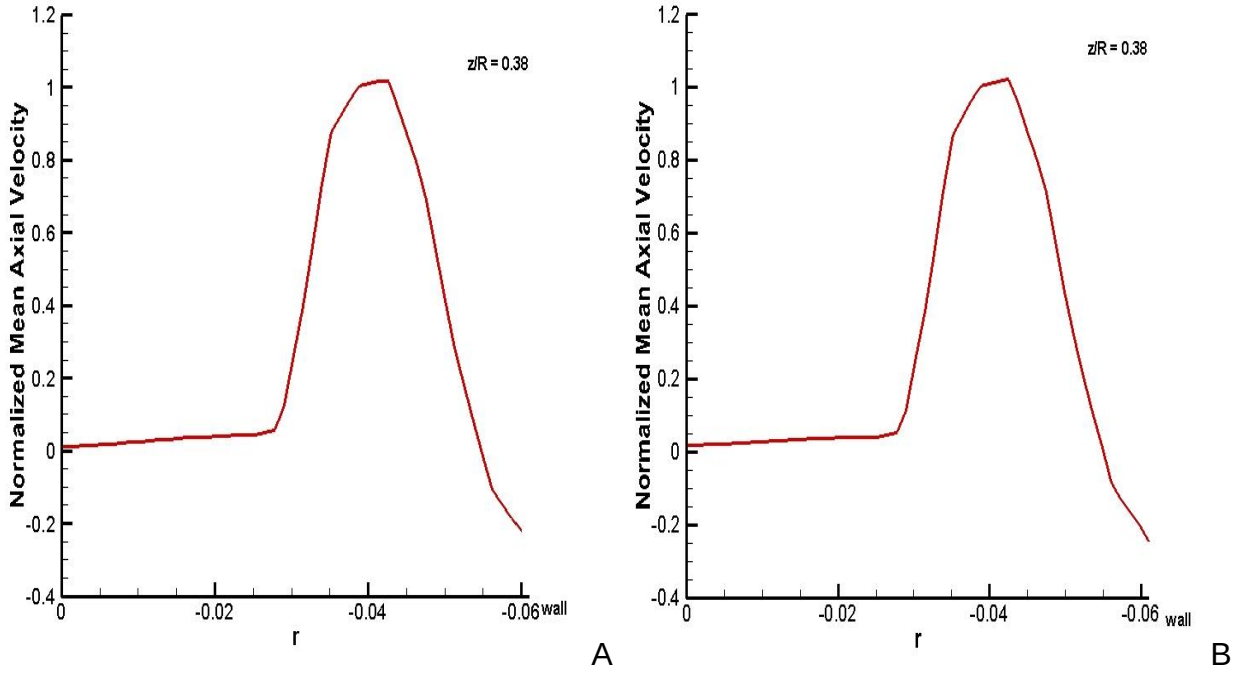

Figure 4-21. Radial profiles of mean axial velocity (m/sec) at z/R = 0.38. A) without plasma, B) with plasma.

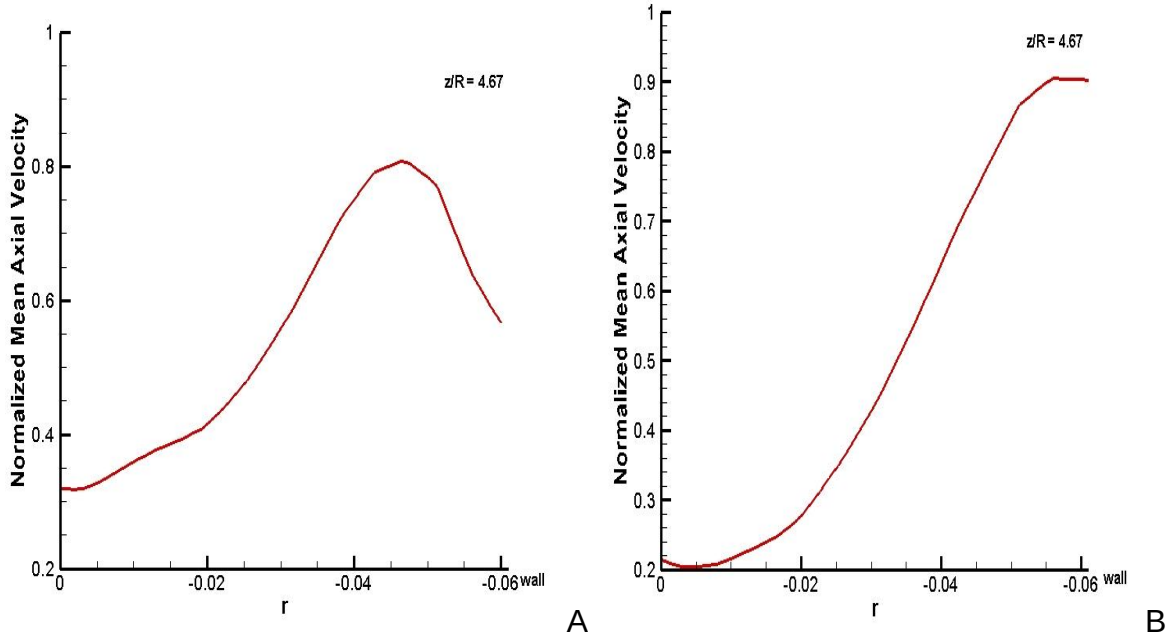

Figure 4-22. Radial profiles of mean axial velocity (m/sec) at z/R = 4.67. A) without plasma, B) with plasma.

Figure 4-18 reveals that there is no big change in the mean temperature profile at z/R = 0.89. This is because there is no effect of plasma on the fluid before the location where plasma generated body force is activated. Figure 4-19 and 4-20 reveal that there is a noticeable change in the mean temperature profile. The peak temperature has reduced from 2150K to 2000K at z/R = 4.52 and from 2175K to 2050K at z/R = 5.20. The minimum temperatures have increased in value and this behavior is observed since there is no external energy added to the system. The curve has become flatter near the center implying that the temperature distribution has become uniform and more homogenous combustion is achieved. This trend is due to the turbulence mixing created by the plasma actuated body force. Reduction in peak temperatures implies a reduction in the amount of NO_x emissions. Moreover, the flame has stretched in the radial direction, since the fuel was directed along the radial direction because of the body force in that direction acting on the adjacent layers. Figure 4-22 indicates that the values of the mean axial velocity near the wall with plasma activation are greater than the values without plasma activation. This is because of the increase in the axial velocity obtained by the acting body force.

4.6 NO_X Emissions

Prediction of nitrogen oxides emissions in gas turbine engines exhausts is important due to strict environmental legislations. Formation of nitrogen oxides is governed by a combination of chemical, thermal and fluid dynamic processes. An empirical correlation has been determined by Louis Tsague et al. [18], between the NO_x emissions index and the flame temperature. The above mentioned empirical relation is not as significant compared to the relations between NO_x emissions index and the

combustor inlet temperature (T_i) and fuel mass flow rate. Relation between flame temperature and NO_x emissions index is given by Equation 4-1.

$$EI_{NO_X} = 2 \times 10^{-83} T_f^{24.696} \quad (4\text{-}1)$$

$$EI_{NO_X} = 4 \times 10^{-9} T_i^{3.364} \quad (4\text{-}2)$$

In the present study, the difference in the amount of NO_x emissions, with and without the operation of plasma, has been obtained. The emissions index has been computed at all the nodal temperatures. The average has been taken for all the index values with the integration performed over the cell volumes. The NO_x emissions index has a value of 0.5931 g/kg fuel when the combustion takes place without plasma and the emissions index value reduced to 0.2894 g/kg fuel with the employment of plasma actuators. NO_x levels have reduced by 51.2 % of the initial concentration. Relation between combustor inlet temperature and the emissions index, given by Equation 4-2 was proved to be more significant than between flame temperature and emissions index, since measurement of flame temperature is complicated and measurement could involve significant errors. The above discussed result does not include the air chemistry reactions, which can lead to a reduction in the amount of NO_x emissions [15].

4.7 Fuel Concentration

Figure 4-23 shows the radial distribution of mean fuel concentration at different axial locations. The peak values in the methane concentration have reduced and the curves have become broader after the application of plasma, implying that the fuel concentration has increased in certain regions. This is due to the fact that the fuel is directed towards the wall because of the body force acting in the outward normal direction in the plasma region. Moreover, Figure 4-23 reveals that the engine can be

operated with lean mixtures resulting in a decrease in the temperature of the combusted products and a subsequent reduction in the amount of nitrogen oxides produced.

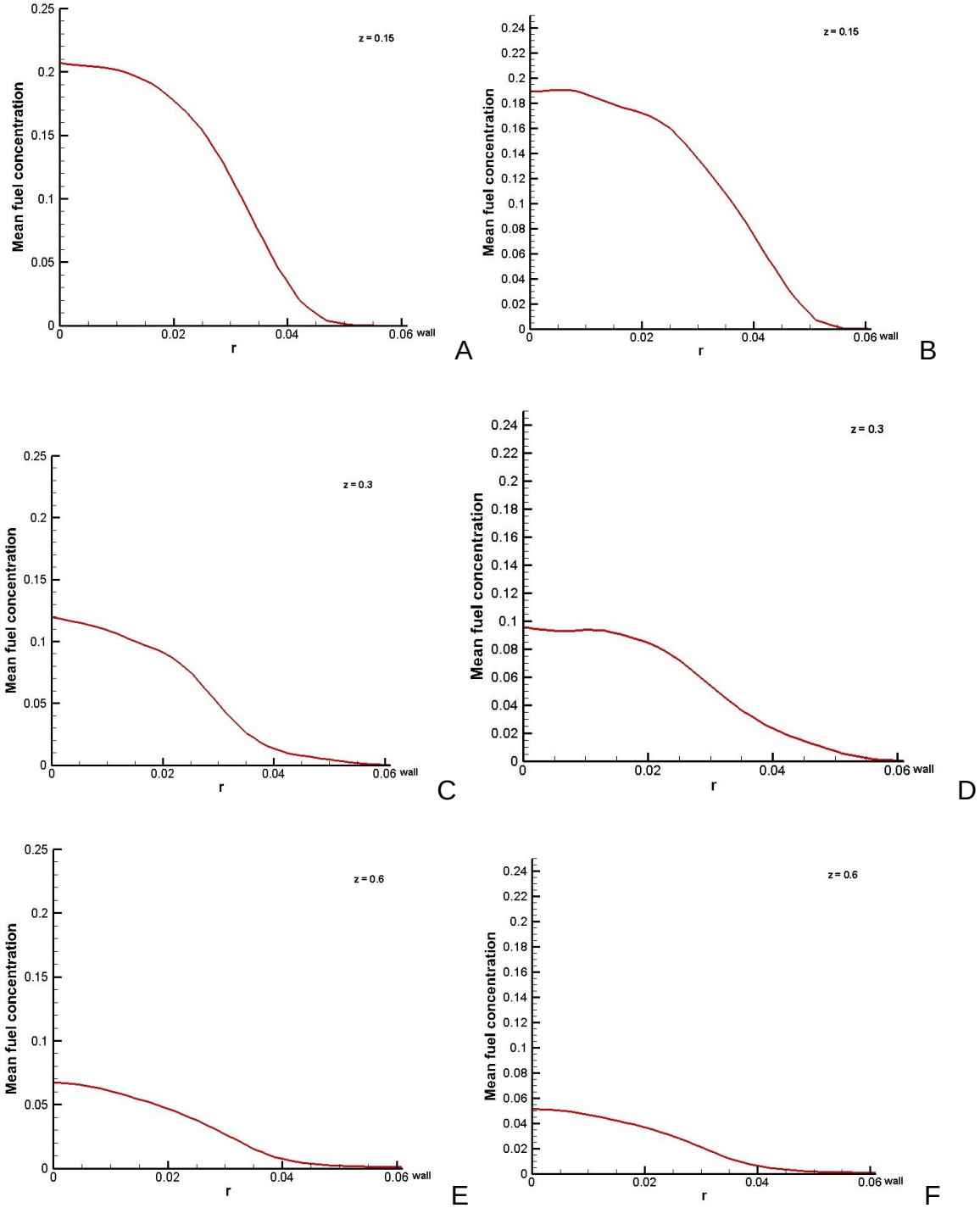

Figure 4-23. Radial distribution of mean fuel concentration at different axial locations. A) z =0.15 without plasma, B) z = 0.15 with plasma, C) z = 0.3 without plasma, D) z = 0.3 with plasma, E) z = 0.6 without plasma, F) z = 0.6 with plasma.

CHAPTER 5
CONCLUSIONS

In the present work, a computational model has been presented to study the effect of plasma actuation on combustion in a gas turbine combustion chamber. All 2D and 3D simulations have been run in FLUENT. Results obtained from the 3D DES model in FLUENT were in good agreement with the results discussed in [17]. Application of plasma actuation generated a body force in the fluid layers underneath the wall which resulted in turbulent mixing and as a result, the flame structure has been modified. All the unsteady simulations were carried out for a sufficiently long time until the mean values have become steady. The important outcomes of this work are listed below:

1. The mean temperature curve near the center line of the combustor has flattened implying a homogenous combustion because of the turbulent mixing.
2. The peak temperatures have been reduced after employing the plasma actuators implying a reduction in the amount of NO_x emissions. This estimate is not as significant as compared to the relation between inlet temperature and the emissions index, since measurement of flame temperatures is complicated and can be measured with significant errors.
3. There was an increment in the mean axial velocity at the near wall regions after activating the plasma actuators.
4. Flame width has increased in the radial direction after enabling the plasma actuators.
5. Mean fuel concentration distribution has been modified.

CHAPTER 6
RECOMMENDATIONS FOR FUTURE STUDY

In the present study, a coaxial jet combustor has been chosen for the simulation with methane as fuel. The present study can be extended to employing of different fuels such as diesel, gasoline, etc. Since these fuels are in liquid state, an atomizer has to be designed for fuel injection. A standard linear plasma actuator has been used in the present study, attached along the circumference of the cylinder at a particular axial location. A different orientation of plasma force can be generated by attaching the plasma actuator on the wall across the length of the combustor at different positions located azimuthally. In this way, a body force is created on the fluid in radial and swirl directions. The number of plasma actuators can be increased in order to aggravate the body force on the fluid. The geometry of the plasma actuator can also be changed in order to study the modification in the combustion phenomenon. Typical geometries of plasma actuators include serpentine, triangular and square. The study can be extended to a more accurate level by employing a much finer grid. This would require a much higher processor speed in order to complete the simulation in a reasonable amount of time.

LIST OF REFERENCES

1. Ryan Durscher and Subrata Roy, “Induced flow from serpentine plasma actuators acting in quiescent air,” AIAA-2011-957, *49th AIAA Aerospace Sciences Meeting and Exhibit*, Orlando, Florida, January 4-7 (2011).

2. Malinovsky, A.E., *J. Chem. Phys*. Paris 21 469 (1924).

3. Calcote, H.F., “Effect of dc Electric Field on Burner Flame,” *Princeton University, Project Squid Technical Report*, (1946).

4. Lesieur, M. & Metais, O., “New trends in large-eddy simulations of turbulence,” *Annu. Rev. Fluid Mech*. 28, 45-82 (1996).

5. Moin, P., “Advances in large eddy simulation methodology for complex flows,” *Intl J. Heat Fluid Flow* 23, 710-720 (2002).

6. Johnson, B.V. and Bennett J. C., “Statistical characteristics of velocity, concentration, mass transport, and momentum transport for coaxial jet mixing in a confined duct,” *J. Engng Gas Turbines and Power* 106, 121-127 (1984).

7. Owen, F. K., Spadaccini, L. J. and Bowman, C. T., “Pollutant formation and energy release in confined turbulent diffusion flames,” *Proc. Combust. Inst*. 16, 105-117 (1976).

8. Akselvoll, K. and Moin, P., “Large-eddy simulation of turbulent confined coannular jets,” *J. Fluid Mech*. 315, 387-411 (1996).

9. Pierce, C.D. and Moin, P., “a Large eddy simulation of a confined coaxial jet with swirl and heat release,” *AIAA Paper* 98-2892 (1998).

10. Ferziger, J., “Large eddy simulation: an introduction and perspective,” In New tools in turbulence modeling, *Les Editions de Physique – Springer Verlag*, pp. 29-47 (1997).

11. Lesieur, M., “Recent approaches in large-eddy simulations of turbulence,” In New tools in turbulence modeling, *Les Editions de Physique – Springer Verlag*, pp. 1-28 (1997).

12. Matveev, I., ”Multi-mode Plasma Igniters and Pilots for Aerospace and Industrial Applications,” 2*-nd Int. Workshop and Exhibition on Plasma Assisted Combustion*, Falls Church, Virginia, pp. 12 (2006).

13. Matveev, I., “Triple Helical Flow Vortex Reactor,” U.S. Patent 7,452,513 B2, Nov. 18 (2008).

14. Sy Stage, Yongho Kim, Vincent Ferreri, Louis Rosocha, A. and Don Coates, M., “Flame Images Indicating Combustion Enhancement by Dielectric Barrier Discharges,” *IEEE Transactions on Plasma Science*, VOL. 33, NO. 2, April (2005).

15. Toshiaki Yamamoto, Chen-Lu Yang, Michael Beltran, R. and Zhorzh Kravets, “ Plasma-Assisted Chemical Process for NO_x Control,” *IEEE Transactions on Industry Applications,* VOL. 36, NO. 3, May/June (2000).

16. Singh, K.P. and Roy, S., “Force approximation for a plasma actuator operating in atmospheric air,” *Journal of Applied Physics* 103, 013305 (2008).

17. Charles D. Pierce and Parviz Moin, “Progress-variable approach for large-eddy simulation of non-premixed turbulent combustion,” *J. Fluid Mech*, vol. 504, pp. 73-97 (2004).

18. Louis Tsague, Thomas Tamo Tatietse, John Ngundam and Joseph Tsogo, “Predictions of emissions in turbojet engines exhausts: relationship between nitrogen oxides emission index (EI_{NOx}) and the operational parameters,” Aerospace Science and Technology 11, 459-463 (2007).

BIOGRAPHICAL SKETCH

Anand Srinivas Ankala was born in Hyderabad, India. Anand completed his Bachelor of Technology in mechanical engineering from National Institute of Technology, Warangal, Andhra Pradesh, India, in May 2009 after which he joined University of Florida to pursue his Master of Science degree in mechanical engineering.

Anand started working towards his master's at the University of Florida from the fall of 2009. Later, he got the opportunity to be a part of the Computational Plasma Dynamics research team under the guidance of Dr. Subrata Roy. Upon completion of his master's in August 2011, Anand plans to continue contributing to the mechanical engineering industry and build on his knowledge and experience.